

RIS-aided Radar Detection Architectures with Application to Low-RCS Targets

Fabiola Colone, Senior Member, IEEE, Filippo Costa, Senior Member, IEEE, Yiding Gao, Chengpeng Hao, Senior Member, IEEE, Linjie Yan, Giuliano Manara, Life Fellow, IEEE, and Danilo Orlando*

Abstract—In this paper, we address the radar detection of low observable targets with the assistance of a reconfigurable intelligent surface (RIS). Instead of using a multistatic radar network as counter-stealth strategy with its synchronization, costs, phase coherence, and energy consumption issues, we exploit a RIS to form a joint monostatic and bistatic configuration that can intercept the energy backscattered by the target along irrelevant directions different from the line-of-sight of the radar. Then, this energy is redirected towards the radar that capitalizes all the backscattered energy to detect the low observable target. To this end, five different detection architectures are devised that jointly process monostatic and bistatic echoes and exhibit the constant false alarm rate property at least with respect to the clutter power. To support the practical implementation, we also provide a guideline for the design of a RIS that satisfies the operating requirements of the considered application. The performance analysis is carried out in comparison with conventional detectors and shows that the proposed strategy leads to effective solutions to the detection of low observable targets.

Index Terms—Adaptive detection, generalized likelihood ratio test, low-RCS targets, maximum likelihood approach, radar, radar cross section, reflective intelligent surface.

I. Introduction

In the recent years, reconfigurable intelligent surfaces (RISs) is a technology that has gained a leading role in the context of new-generation wireless communications [1], [2, and references therein]. These surfaces can be broadly categorized into passive smart electromagnetic skins or reflectarrays, which provide fixed beamforming and fully reconfigurable versions capable of dynamic wave control [3]. Their real-time programmability is enabled by semiconductor elements such as PIN and varactor diodes [4], enabling manipulation of phase, amplitude, and polarization [5]. Advanced architectures integrate sensing

The work of D. Orlando was partially supported by the Italian Ministry of Education and Research (MUR) in the framework of the FoReLab project (Departments of Excellence).

F. Colone is with the Department of Information Engineering, Electronics and Telecommunications, Sapienza University of Rome, 00184 Rome, Italy. E-mail: fabiola.colone@uniroma1.it.

F. Costa, G. Manara, and D. Orlando are with the Department of Information Engineering, Università di Pisa, Via Caruso 16, 56122 Pisa, Italy. E-mail: filippo.costa@unipi.it; giuliano.manara@unipi.it; danilo.orlando@unipi.it.

Y. Gao, C. Hao, and L. Yan are with the Institute of Acoustics, Chinese Academy of Sciences, Beijing 100190, China, and also with the School of Electronic, Electrical and Communication Engineering, University of Chinese Academy of Sciences, Beijing 100049, China. E-mail: gaoyiding@mail.ioa.ac.cn; haochengp@mail.ioa.ac.cn; yanlinjie16@163.com.

*Corresponding author

functions [6], or active components to compensate for double-path loss [7]. This hardware versatility positions RIS as a cornerstone for smart programmable radio environments in 5G-Advanced and 6G networks.

Although the use of the RIS originates in the field of communication networks, its extension to sensing systems is making great strides with the advent of integrated sensing and communication (ISAC) paradigm in urban scenarios [8]. As a matter of fact, in this respect, many excellent contributions can be found in the open literature focused on different levels of coexistence, cooperation, or codesign of the sensing and communication systems. In [9], a design framework for the coexistence of multiple-input multiple-output (MIMO) radar and communication systems is devised by exploiting the assistance of a RIS. The codesign metric is the signal-to-interference-plus-noise ratio (SINR) that is optimized to enhance the target detection capability of the radar system and to guarantee the communication quality of service. Other codesign approaches can be found in [10], [11] where the RIS is used to mitigate the mutual interference between the sensing and communication systems. A dual-function radar-communication system is proposed in [12], where in place of conventional RISs the so-called hybrid RISs are used to enhance the amount of received energy backscattered by the target. The fundamental trade-offs for the design of the radar and communication functions are investigated to maximize the SINR of the radar while satisfying the SINR requirements on the communication side. In the context of 5G/6G, in [13], an orthogonal frequency division multiplexing based ISAC system is proposed where a RIS is used by the base station for the detection of non-cooperative small targets with low radar cross section (RCS). To this end, the system integrates multiple frames and the track-before-detect [14], [15] paradigm is applied to account for target motion. The use of RIS capable of modulating the polarization is investigated in [16] to obtain an improvement in target classification for a distributed MIMO ISAC system.

A parallel research line investigates the application of RIS to radar systems only operating in scenarios that possibly go beyond those for communications. An important contribution is provided in [17], where the authors focus on the system design and carry out a theoretical analysis of the main design aspects including signal bandwidth, carrier frequency, RIS size, and relative distance between radar and RIS. The application proposed in [18] considers

a radar system operating in a urban scenario where there exist regions for which the line-of-sight (LOS) condition is not valid. In these environments, the RIS comes into play to cover the blind regions. The same application is addressed in [19] where optimal phase shifts for the RIS are computed for each pointing direction belonging to the angular sector of interest. In [20], a general signal model for a radar system assisted by RIS is derived by encompassing the LOS and non-LOS conditions. This model is used to optimize RIS deployment and for the design of the transmit waveforms, receive filters, and RIS phase shifts. The non-LOS condition is still considered in [21], where multiple RISs are used to assist a monostatic radar. Specifically, the authors investigate the effects on the detection performance generated by additional RISs under the non-LOS condition. A novel radar architecture is developed in [22], where, in addition to the monostatic echoes, the radar system collects bistatic echoes reflected by the RIS. This approach allows for the exploitation of the spatial diversity (on receive) to enhance the system detection capabilities. Notice that the radar is assumed to illuminate the target only and not also the RIS. The potential of RIS in the context of MIMO radars is explored in [23] where the devised system processes the returns from (up to) two RISs deployed in the region of interest. The RIS phase shifts are computed in order to maximize the probability of detection (P_d) for a given probability of false alarm (P_{fa}) by means of the maximum likelihood approach. Other interesting contributions can be found in [24]–[26].

This paper is framed in the second of the two lines of research described above, namely the development of RIS-aided radar systems. Remarkably, it focuses for the first time (at least to the best of authors' knowledge) on the design of detection architectures for airborne targets designed to exhibit a low-RCS. Otherwise stated, the low-RCS is not due to the target size as assumed in [13] but it is a design objective. As a matter of fact, in the last decades, stealth or “low observable” technology has proven to be one of the most effective approaches to hide targets from radar systems [27]. Especially in the defense context, all new aircraft are designed taking into account low observable principles and techniques, while the project of existing platforms is reconsidered to reduce the corresponding radar signature. As explained in Section V, a design principle of low-RCS platforms consists in shaping the platform to reduce the backscattered energy in a specific angular sector (mainly related to the frontal aspect). More precisely, most of the intercepted energy is redirected towards irrelevant directions. Notice that multistatic radar systems represent an effective means to counter the stealth technology since they use spatial diversity to intercept the energy reflected towards the aforementioned irrelevant directions.

Thus, the main idea behind this paper is that a monostatic radar can exploit suitably deployed RISs to form bistatic configurations capable of intercepting the energy backscattered by the target along directions dif-

ferent from the LOS. Unlike [22], here the RIS is placed within the mainbeam of the radar system. This idea has a significant practical value since the use of the RIS allows for lower costs than a multistatic radar network with its synchronization, phase coherence, and energy consumption issues. The RIS is designed and deployed to recover a sufficient level of energy that can trigger the detection of a low observable target. To this end, the RIS backscattering pattern is statically designed to illuminate all the radar cells under investigation simultaneously with a single, fixed beam. This is achieved through an adequate, pre-defined tapering of the surface's unit cells to control both the phase and amplitude of the reflected wavefront. It is clear that the RIS can be reconfigured to illuminate different batch of range cells. Moreover, we investigate the requirements related to the geometry of the scenario assuming a search radar with a fan beam, which also illuminates the RIS, and provide a formal statement of the detection problem that accounts for these requirements. Such a problem appears here for the first time (at least to best of authors' knowledge) and is solved by applying design criteria based upon the generalized likelihood ratio test (GLRT) [28] and ad hoc modifications of it. To be more definite, since the joint maximization of the likelihood function with respect to the entire set of unknown parameters is a difficult task from a mathematical point of view, we resort to alternative approaches based upon either

- the estimate-and-plug paradigm [29]–[31] that computes the GLRT assuming that a subset of parameters is known and then replaces these parameters with suitable estimates;
- an approximate solution for the GLRT obtained by minimizing an upper bound to the objective function;
- an iterative optimization procedure that leads to (at least) local stationary points.

Thus, we obtain five different detection architectures and theoretically show that they exhibit the constant false alarm rate (CFAR) property with respect to the clutter power in a clutter-dominated environment. As for the CFAR property with respect to the covariance structure, we also prove that they are bounded from above by decision statistics functionally invariant to the covariance structure. Finally, we provide both a technical description of low-RCS target features and the guidelines to design a RIS whose task is the interception of the energy from the irrelevant directions. The performance analysis, conducted on synthetic data and in comparison with conventional detectors, clearly shows that the proposed approach is an effective means to detect low-RCS targets with significant performance gains over the considered counterparts.

The remainder of the paper is organized as follows. In the next section, the operating requirements are described and the detection problem is formulated in terms of a binary hypothesis test. Section III is devoted to the design of the detection architectures along with the related estimation procedures. The analysis of the CFAR

behavior is conducted in Section VI-B, while Section V is devoted to the design of the RIS according to the energy requirements for low observable targets. Finally, the performance assessment is confined to Section VI and some concluding remarks are provided in Section VII.

A. Notation

In the sequel, vectors and matrices are denoted by bold-face lower-case and upper-case letters, respectively. The (i, j) th entry of a matrix \mathbf{A} is indicated by $\mathbf{A}(i, j)$. Symbols $\det(\cdot)$, $\text{Tr}(\cdot)$, $(\cdot)^T$, and $(\cdot)^\dagger$ denote the determinant, trace, transpose, and conjugate transpose, respectively. As to the numerical sets, \mathbb{C} is the set of complex numbers and $\mathbb{C}^{N \times M}$ is the Euclidean space of $(N \times M)$ -dimensional complex matrices (or vectors if $M = 1$). For two sets A and B , the difference set is $A \setminus B$. Function $\text{rect}(x)$ is the rectangular window and is equal to 1 if $|x| < 1/2$ and to 0 if $|x| > 1/2$. \mathbf{I} and $\mathbf{0}$ stand for the identity matrix and the null vector or matrix of proper size. Given $\mathbf{a} \in \mathbb{C}^{N \times 1}$, $\text{diag}(\mathbf{a}) \in \mathbb{C}^{N \times N}$ indicates a diagonal matrix whose i th diagonal element is the i th entry of \mathbf{a} . If $\mathbf{A} \in \mathbb{C}^{N \times N}$, $\text{diag}(\mathbf{A}) \in \mathbb{C}^{N \times N}$ is a diagonal matrix whose main diagonal is the same as \mathbf{A} . Symbol $\|\cdot\|_F$ is the Frobenius norm of the matrix argument. The acronym PDF stands for Probability Density Function. Finally, we write $\mathbf{x} \sim \mathcal{CN}_N(\mathbf{m}, \mathbf{M})$ if \mathbf{x} is a complex circular N -dimensional normal vector with mean \mathbf{m} and positive definite covariance matrix \mathbf{M} , whereas $\mathbf{X} \sim \mathcal{CW}_N(K, \mathbf{A})$ means that matrix $\mathbf{X} \in \mathbb{C}^{N \times N}$ obeys the complex Wishart distribution with parameters K and $\mathbf{A} \in \mathbb{C}^{N \times N}$.

II. Problem Formulation

Let us consider a monostatic radar system that uses a planar array of N_a tiles to sense the region of interest. The system transmits a coherent burst of N_p pulses that are Doppler tolerant [32] and the illumination is accomplished by means of a fan beam.¹ A RIS is placed in the region of interest with the objective of illuminating prospective stealth targets from below as depicted in Figure 1, where $d_{RS} > 0$ is the RIS-radar distance, $d_{RT} > 0$ is the distance from the radar to the target, and $d_{ST} > 0$ is the distance between the target and the RIS. The RIS configuration is such that it can manage the path radar-RIS-target and target-RIS-radar. The prospective target is shaped in order to exhibit a low radar cross section along the flight direction, namely its surfaces and edges deflect the scattered energy in directions away from the monostatic radar [33], [34]. It is clear that this behavior cannot be forced for all angles of view and there will always exist aspect angles at which the target surfaces generate high-energy echoes. Since many stealth vehicles mainly minimize radar echo in the head-on direction, a bistatic configuration might allow for the interception the echoes reflected towards directions that are different from that to

¹The beam shape can be obtained by a suitable tapering of the spatial channels or by using a subset of sensors along the elevation dimension.

the electromagnetic source (i.e., the radar system). Thus, the deployment of a RIS, which is passive and, hence, low observable, within the region of interest provides spatial diversity and leads to a bistatic configuration that can be considered a counter-stealth technology.

To be more definite, let us consider Figure 2 where the most significant routes taken by the received echoes are shown (other possible paths are neglected). In the figure, the delays τ_i , $i = 1, 2, 3$, associated with each path are defined as

$$\begin{cases} \tau_1 = \frac{2d_{RT}}{c}, \\ \tau_2 = \frac{d_{RT} + d_{ST} + d_{RS}}{c}, \\ \tau_3 = \frac{2(d_{RS} + d_{ST})}{c}, \end{cases} \quad (1)$$

where c is the speed of light. For future reference, we denote the paths associated with τ_1 , τ_2 , and τ_3 with radar-target-radar (RTR), radar-target-surface-radar (RTSR), and radar-surface-target-surface-radar (RSTS), respectively. Notice that also the path radar-surface-target-radar (RSTR) is associated with τ_2 . Since the operating scenario is dynamic, for a target approaching the radar, we can assume that the following inequalities hold

$$\begin{cases} \tau_3 - \tau_1 = \frac{2(d_{RS} + d_{ST} - d_{RT})}{c} \geq \frac{4\Delta r}{c} > 0, \\ \tau_3 - \tau_2 = \frac{d_{RS} + d_{ST} - d_{RT}}{c} \geq \frac{2\Delta r}{c} > 0, \\ \tau_2 - \tau_1 = \frac{d_{RS} + d_{ST} - d_{RT}}{c} \geq \frac{2\Delta r}{c} > 0, \end{cases} \quad (2)$$

where Δr is the radar range resolution. In fact, in the presence of an airborne target approaching the radar, the above conditions can be met for a likely geometry. For instance, if $d_{RT} = 19000$ m, $d_{RS} = 20000$ m, $d_{ST} = 1000$ m, and $\Delta r = 50$ m, then $\tau_1 \approx 126 \mu\text{s}$, $\tau_2 \approx 133 \mu\text{s}$, $\tau_3 \approx 140 \mu\text{s}$, and $2\Delta r/c \approx 0.3 \mu\text{s}$. The delay differences are $\tau_3 - \tau_1 \approx 14 \mu\text{s}$, $\tau_3 - \tau_2 \approx 7 \mu\text{s}$, and $\tau_2 - \tau_1 \approx 7 \mu\text{s}$; all of them are one order of magnitude greater than $2\Delta r/c$ satisfying the conditions (2). As a consequence, if we denote by k_1 the index of the range bin containing the echoes corresponding to τ_1 , the reflected signal exhibiting the delay τ_2 occupies the range cell indexed by $k_2 > k_1$, whereas the echoes with delay τ_3 are present in the range bin indexed by $k_3 > k_2$. Actually, all conditions (2) are satisfied if

$$d_{RS} + d_{ST} - d_{RT} \geq 2\Delta r. \quad (3)$$

With the above remarks in mind, we jointly process a set of K_P consecutive range bins (forming the window under test), where the first cell is associated with τ_1 and two out of $K_P - 1$ range bins are related to τ_2 and τ_3 . The remaining range bins are assumed free of signal components. Moreover, we assume the availability of the conventional set of training samples to estimate the unknown statistical parameters of the disturbance.²

²In what follows, we consider a clutter dominated environment.

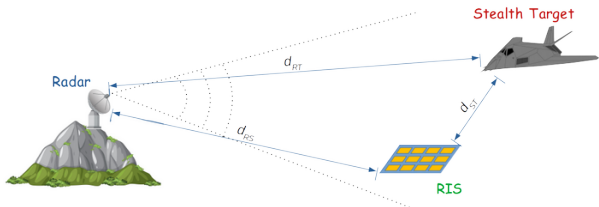


Fig. 1: Geometry of the operating scenario.

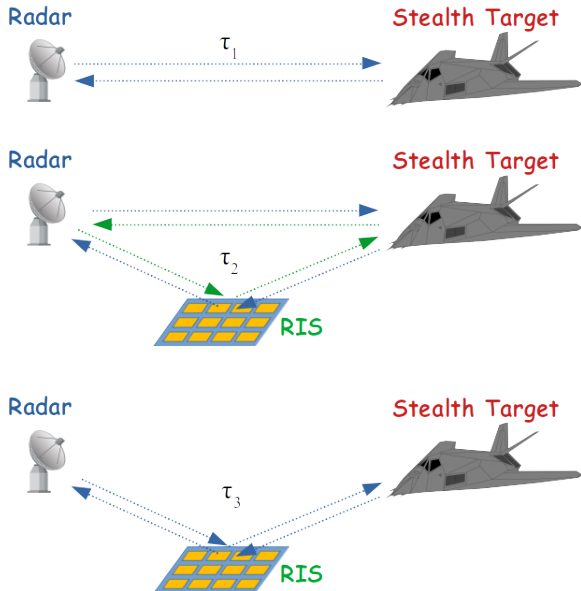


Fig. 2: Considered paths.

Summarizing, the detection problem of interest can be formulated as the following binary hypothesis test

$$\left\{ \begin{array}{l} H_0 : \begin{cases} \mathbf{z}_k \sim \mathcal{CN}_N(\mathbf{0}, \mathbf{M}), & k \in \Omega_P, \\ \mathbf{r}_k \sim \mathcal{CN}_N(\mathbf{0}, \mathbf{M}), & k \in \Omega_S, \end{cases} \\ H_1 : \begin{cases} \mathbf{z}_1 \sim \mathcal{CN}_N(\alpha_1 \mathbf{v}_R, \mathbf{M}), \\ \mathbf{z}_n \sim \mathcal{CN}_N(\alpha_n \mathbf{v}_{SR}, \mathbf{M}), & n \in \Omega_P, n > 1, \\ \mathbf{z}_m \sim \mathcal{CN}_N(\alpha_m \mathbf{v}_S, \mathbf{M}), & m \in \Omega_P, m > n, \\ \mathbf{z}_k \sim \mathcal{CN}_N(\mathbf{0}, \mathbf{M}), & k \in \Omega_P \setminus \{1, n, m\}, \\ \mathbf{r}_k \sim \mathcal{CN}_N(\mathbf{0}, \mathbf{M}), & k \in \Omega_S, \end{cases} \end{array} \right. \quad (4)$$

where the condition $m > n$ makes it possible to account for effects due to both propagation and fast-time sampling anomalies,

- $\mathbf{z}_k \in \mathbb{C}^{N \times 1}$, $k \in \Omega_P = \{1, \dots, K_P\}$, are the space-time vectors (with $N = N_a N_p$ the number of space-time channels) containing the echo samples from the window under test,³ which contains the signals traveling according to the previously mentioned paths; we denote by $\mathbf{Z}_P = [\mathbf{z}_1, \dots, \mathbf{z}_{K_P}] \in \mathbb{C}^{N \times K_P}$ the overall primary data matrix;

³The incoming signals undergo the conventional operations of down-conversion, matched filtering, and fast-time sampling.

- $\mathbf{r}_k \in \mathbb{C}^{N \times 1}$, $k \in \Omega_S = \{1, \dots, K_S\}$ with $K_S \geq N$,⁴ are the training vectors assumed free of useful signal components and statistically independent of $\mathbf{z}_1, \dots, \mathbf{z}_{K_P}$; we denote by $\mathbf{R} = [\mathbf{r}_1, \dots, \mathbf{r}_{K_S}] \in \mathbb{C}^{N \times K_S}$ the overall secondary data matrix;
- $\mathbf{v}_R \in \mathbb{C}^{N \times 1}$ is the known space-time target steering vector as seen by the radar and, hence, is a function of target azimuth angle, elevation angle, and monostatic Doppler frequency (computed with respect to the radar);
- $\mathbf{v}_{SR} = \mathbf{v}_{S,1} + \mathbf{v}_{R,1}$ is the composition between the steering vectors associated with each path corresponding to τ_2 (see Figure 2); specifically, $\mathbf{v}_{S,1} \in \mathbb{C}^{N \times 1}$ is the steering vector associated with the path RTSR and $\mathbf{v}_{R,1} \in \mathbb{C}^{N \times 1}$ the steering vector corresponding to the path RSTR, both characterized by the same bistatic Doppler frequency but different angles of arrival;
- $\mathbf{v}_S \in \mathbb{C}^{N \times 1}$ is the known space-time target signature of the RIS with respect to the radar when it reflects target echoes (in this case azimuth and elevation angles are those of the RIS while Doppler frequency depends on the target radial velocity with respect to the RIS);
- $\alpha_1 \in \mathbb{C}$, $\alpha_n \in \mathbb{C}$, and $\alpha_m \in \mathbb{C}$ are the unknown target responses, which also include channel and system effects, corresponding to the paths RTR, RTSR (RSTR), and RSTSR, respectively;
- $\mathbf{M} \in \mathbb{C}^{N \times N}$ is the unknown positive definite covariance matrix of the disturbance.

The subsequent derivations require the expressions of the joint PDFs of \mathbf{Z}_P and \mathbf{R} under each hypothesis. Specifically, denoting by $K = K_P + K_S$ the total number of vectors, the PDFs under H_0 and H_1 can be written as

$$f(\mathbf{Z}_P, \mathbf{R}; \mathbf{M}, H_0) = \frac{\exp\{-\text{Tr}[\mathbf{M}^{-1}(\mathbf{S}_P + \mathbf{S}_S)]\}}{\pi^{KN} \det^K(\mathbf{M})} \quad (5)$$

and

$$\begin{aligned} f(\mathbf{Z}_P, \mathbf{R}; \boldsymbol{\alpha}, n, m, \mathbf{M}, H_1) = & \frac{1}{\pi^{KN} \det^K(\mathbf{M})} \\ & \exp \left\{ -\text{Tr} \left[\mathbf{M}^{-1} \left((\mathbf{Z}_{1,n,m} - \mathbf{V}\mathbf{A}) \right. \right. \right. \\ & \left. \left. \times (\mathbf{Z}_{1,n,m} - \mathbf{V}\mathbf{A})^\dagger + \mathbf{S}_{n,m} \right) \right] \right\}, \end{aligned} \quad (6)$$

respectively, where $\mathbf{S}_P = \mathbf{Z}_P \mathbf{Z}_P^\dagger$, $\mathbf{S}_S = \mathbf{R} \mathbf{R}^\dagger$,

$$\mathbf{S}_{n,m} = \mathbf{S}_S + \sum_{k \in \Omega_P \setminus \{1, n, m\}} \mathbf{z}_k \mathbf{z}_k^\dagger, \quad (7)$$

$\mathbf{Z}_{1,n,m} = [\mathbf{z}_1, \mathbf{z}_n, \mathbf{z}_m] \in \mathbb{C}^{N \times 3}$, $\boldsymbol{\alpha} = [\alpha_1, \alpha_n, \alpha_m]^T \in \mathbb{C}^{3 \times 1}$, $\mathbf{A} = \text{diag}(\boldsymbol{\alpha})$, and⁵ $\mathbf{V} = [\mathbf{v}_R, \mathbf{v}_{SR}, \mathbf{v}_S] \in \mathbb{C}^{N \times 3}$. Notice that in the case of space-time processing and assuming

⁴This condition is required to make the sample covariance matrix based upon $\mathbf{r}_1, \dots, \mathbf{r}_{K_S}$ nonsingular with probability 1.

⁵For simplicity, we have omitted the dependence of $\boldsymbol{\alpha}$ on (n, m) .

that the bistatic Doppler is different from the monostatic Doppler, \mathbf{V} is full-column rank.⁶

In the next section, we devise detection architectures for problem (4) by exploiting the GLRT design paradigm and suitable modifications of it that allow us to overcome possible intractable mathematics.

III. Architecture Designs

The general formulation of the GLRT for problem (4) is

$$\frac{\max_{\substack{n, m \in \Omega_P \\ n > 1, m > n}} \max_{\boldsymbol{\alpha}} \max f(\mathbf{Z}_P, \mathbf{R}; \boldsymbol{\alpha}, n, m, \mathbf{M}, H_1)}{\max_{\mathbf{M}} f(\mathbf{Z}_P, \mathbf{R}; \mathbf{M}, H_0)} \stackrel{H_1}{\underset{H_0}{\gtrless}} \eta, \quad (8)$$

where η is the detection threshold whose value depends on the P_{fa} specified by system requirements.⁷ The maximization at the denominator is a well-known problem that has been addressed in a plethora of available contributions (see for instance [30], [35]–[41] and references therein). Thus, for brevity, we recall here that the expression of the compressed likelihood function under H_0 is⁸

$$f(\mathbf{Z}_P, \mathbf{R}; \widehat{\mathbf{M}}, H_0) = \left[\frac{K}{\pi e \det^{1/N}(\mathbf{S}_P + \mathbf{S}_S)} \right]^{KN} \quad (9)$$

and it will be used in the next subsections when required.

On the other hand, the optimization of the likelihood function under H_1 (i.e., the numerator of (8)) is involved from a mathematical point of view and, hence, we resort to suboptimal modifications of the maximum likelihood approach to come up with suitable estimates of the unknown parameters. In the next subsections, we describe these modifications that lead to different decision schemes.

A. Estimate-and-Plug Solutions

The approach used in this subsection (also known as two-step GLRT [29]) consists in deriving the GLRT when a subset of parameters are known. As a consequence, the resulting decision statistic is a function of such parameters. To make it adaptive, the remaining parameters are replaced by suitable estimates.

Let us start by considering the following steps

1) compute the GLR for known \mathbf{M} , that is

$$\frac{\max_{\substack{n, m \in \Omega_P \\ n > 1, m > n}} \max_{\boldsymbol{\alpha}} f(\mathbf{Z}_P, \mathbf{R}; \boldsymbol{\alpha}, n, m, \mathbf{M}, H_1)}{f(\mathbf{Z}_P, \mathbf{R}; \mathbf{M}, H_0)}; \quad (10)$$

2) replace \mathbf{M} with a suitable estimate obtained from the available data (a point better explained below).

⁶In the ensuing derivations, this assumption is required to come up with closed form estimates. However, as we will see, the final decision statistics are independent of this assumption and, hence, they can be also used for space processing only.

⁷Hereafter, we denote by η the generic detection threshold for each architecture.

⁸The term compressed means that the likelihood function has been maximized with respect to the unknown parameters.

Thus, given $n > 1$ and $m > n$, the maximization with respect to $\boldsymbol{\alpha}$ is tantamount to

$$\min_{\boldsymbol{\alpha}} \text{Tr} \left\{ \mathbf{M}^{-1} [(\mathbf{Z}_{1,n,m} - \mathbf{V}\mathbf{A})(\mathbf{Z}_{1,n,m} - \mathbf{V}\mathbf{A})^\dagger] \right\}, \quad (11)$$

where the objective function is convex. Thus, it is not difficult to show that setting to zero the gradient with respect to $\boldsymbol{\alpha}$, we come up with the following minimizers

$$\hat{\alpha}_1(\mathbf{M}) = \frac{\mathbf{v}_R^\dagger \mathbf{M}^{-1} \mathbf{z}_1}{\mathbf{v}_R^\dagger \mathbf{M}^{-1} \mathbf{v}_R}, \quad (12)$$

$$\hat{\alpha}_n(\mathbf{M}) = \frac{\mathbf{v}_{SR}^\dagger \mathbf{M}^{-1} \mathbf{z}_n}{\mathbf{v}_{SR}^\dagger \mathbf{M}^{-1} \mathbf{v}_{SR}}, \quad (13)$$

$$\hat{\alpha}_m(\mathbf{M}) = \frac{\mathbf{v}_S^\dagger \mathbf{M}^{-1} \mathbf{z}_m}{\mathbf{v}_S^\dagger \mathbf{M}^{-1} \mathbf{v}_S}. \quad (14)$$

Replacing these estimates in (10) and taking the natural logarithm, we obtain the following statistically equivalent test

$$\max_{\substack{n, m \in \Omega_P \\ n > 1, m > n}} \left\{ \frac{|\mathbf{v}_R^\dagger \mathbf{M}^{-1} \mathbf{z}_1|^2}{\mathbf{v}_R^\dagger \mathbf{M}^{-1} \mathbf{v}_R} + \frac{|\mathbf{v}_{SR}^\dagger \mathbf{M}^{-1} \mathbf{z}_n|^2}{\mathbf{v}_{SR}^\dagger \mathbf{M}^{-1} \mathbf{v}_{SR}} \right. \\ \left. + \frac{|\mathbf{v}_S^\dagger \mathbf{M}^{-1} \mathbf{z}_m|^2}{\mathbf{v}_S^\dagger \mathbf{M}^{-1} \mathbf{v}_S} \right\} \stackrel{H_1}{\underset{H_0}{\gtrless}} \eta. \quad (15)$$

The plug step is accomplished by replacing \mathbf{M} with \mathbf{S}_S (that is K times the maximum likelihood estimate of \mathbf{M} over \mathbf{R}) or $\mathbf{S}_{n,m}$ (see (7)). Finally, the maximization with respect to (n, m) is numerically conducted over a grid of points. In what follows, we refer to (15) coupled with \mathbf{S}_S as estimate-and-plug GLRT for known \mathbf{M} solution 1 (EP-GLRT-KM-1), while (15) coupled with $\mathbf{S}_{n,m}$ is called estimate-and-plug GLRT for known \mathbf{M} solution 2 (EP-GLRT-KM-2).

As an alternative strategy, instead of considering \mathbf{M} known, we can assume that $\boldsymbol{\alpha}$ is given. Thus, the modified procedure consists of the following steps

1) compute the GLR for known $\boldsymbol{\alpha}$, that is

$$\frac{\max_{\substack{n, m \in \Omega_P \\ n > 1, m > n}} \max_{\boldsymbol{\alpha}} f(\mathbf{Z}_P, \mathbf{R}; \boldsymbol{\alpha}, n, m, \mathbf{M}, H_1)}{\max_{\mathbf{M}} f(\mathbf{Z}_P, \mathbf{R}; \mathbf{M}, H_0)}; \quad (16)$$

2) replace the entries of $\boldsymbol{\alpha}$ with suitable estimates.

Thus, given $n > 1$ and $m > n$, the maximization with respect to \mathbf{M} under H_1 leads to⁹

$$f(\mathbf{Z}_P, \mathbf{R}; \boldsymbol{\alpha}, n, m, \widehat{\mathbf{M}}, H_1) \\ = \left[\frac{K}{\pi e \det^{1/N}(\mathbf{Y}_{1,n,m} + \mathbf{S}_{n,m})} \right]^{KN}, \quad (17)$$

where $\mathbf{Y}_{1,n,m} = (\mathbf{Z}_{1,n,m} - \mathbf{V}\mathbf{A})(\mathbf{Z}_{1,n,m} - \mathbf{V}\mathbf{A})^\dagger$. Exploiting (17) and (9), the GLRT for known $\boldsymbol{\alpha}$ can be

⁹We omit the derivation as it is similar to that under H_0 .

equivalently recast as

$$\max_{\substack{n,m \in \Omega_P \\ n > 1, m > n}} \frac{\det(\mathbf{S}_P + \mathbf{S}_S)}{\det[\mathbf{S}_{n,m} + \mathbf{Y}_{1,n,m}]} \stackrel{H_1}{>} \stackrel{H_0}{<} \eta \quad (18)$$

and the adaptive GLRT is obtained by replacing $\boldsymbol{\alpha}$ with

$$\hat{\boldsymbol{\alpha}} = \begin{bmatrix} \hat{\alpha}_1(\mathbf{S}_S) \\ \hat{\alpha}_n(\mathbf{S}_S) \\ \hat{\alpha}_m(\mathbf{S}_S) \end{bmatrix}. \quad (19)$$

In what follows, we refer to this detector as estimate-and-plug GLRT for known $\boldsymbol{\alpha}$ (EP-GLRT-KA).

B. GLRT based on Cyclic Optimization

The estimation procedure of the unknown parameters under H_1 described in this subsection is grounded on cyclic optimization strategies that lead to a nondecreasing sequence of likelihood values [42]. Specifically, let us focus again on the numerator of (8) and solve the maximization with respect to \mathbf{M} . The partially-compressed likelihood function is further optimized by repeating an iteration formed by the following steps until a stopping criterion is not satisfied

- 1) assume that α_n and α_m are known and equal to the estimates obtained in the previous iteration, then maximize the partially-compressed likelihood with respect to α_1 ;
- 2) let α_1 be equal to the estimate obtained in the previous step and assume again that α_m is equal to the value in the previous iteration, then maximize the partially-compressed likelihood with respect to α_n ;
- 3) assume that α_1 and α_n are equal to the estimates obtained in the steps 1 and 2, respectively, and maximize the partially-compressed likelihood with respect to α_m .

Denoting by $g(\alpha_1, \alpha_n, \alpha_m) = f(\mathbf{Z}_P, \mathbf{R}; \boldsymbol{\alpha}, n, m, \widehat{\mathbf{M}}, H_1)$ the partially-compressed likelihood function (with respect to \mathbf{M}), iterating the above steps leads to the following inequality chain

$$\begin{aligned} g(\alpha_1^{(h-1)}, \hat{\alpha}_n^{(h-1)}, \hat{\alpha}_m^{(h-1)}) &\leq g(\hat{\alpha}_1^{(h)}, \hat{\alpha}_n^{(h-1)}, \hat{\alpha}_m^{(h-1)}) \\ &\leq g(\hat{\alpha}_1^{(h)}, \hat{\alpha}_n^{(h)}, \hat{\alpha}_m^{(h-1)}) \leq g(\hat{\alpha}_1^{(h)}, \hat{\alpha}_n^{(h)}, \hat{\alpha}_m^{(h)}) \\ &\leq g(\hat{\alpha}_1^{(h+1)}, \hat{\alpha}_n^{(h)}, \hat{\alpha}_m^{(h)}) \leq \dots, \end{aligned} \quad (20)$$

where h is the iteration index, $\hat{\alpha}_i^{(h-1)}$, $i \in \{n, m\}$, are the estimation updates in the $(h-1)$ th iteration, $\hat{\alpha}_1^{(h)}$ is obtained through step 1, $\hat{\alpha}_n^{(h)}$ is obtained by means of step 2, and $\hat{\alpha}_m^{(h)}$ comes from step 3. As for the stopping criterion, let us define

$$\begin{aligned} \mathcal{G}(\hat{\alpha}_1^{(h)}, \hat{\alpha}_n^{(h)}, \hat{\alpha}_m^{(h)}) \\ = \frac{g(\hat{\alpha}_1^{(h)}, \hat{\alpha}_n^{(h)}, \hat{\alpha}_m^{(h)}) - g(\hat{\alpha}_1^{(h-1)}, \hat{\alpha}_n^{(h-1)}, \hat{\alpha}_m^{(h-1)})}{g(\hat{\alpha}_1^{(h-1)}, \hat{\alpha}_n^{(h-1)}, \hat{\alpha}_m^{(h-1)})}, \end{aligned} \quad (21)$$

then, a possible choice is

$$0 \leq \mathcal{G}(\hat{\alpha}_1^{(h)}, \hat{\alpha}_n^{(h)}, \hat{\alpha}_m^{(h)}) < \epsilon, \quad (22)$$

or $h \leq h_{\max}$, where h_{\max} is the maximum allowed number of iterations and $\epsilon > 0$. Parameters h_{\max} and ϵ can be set according to computational and performance requirements.

Therefore, to find the expression of the estimation updates, we apply (for computational convenience) the logarithm to the partially-compressed likelihood function and consider

$$\begin{aligned} \log g(\alpha_1, \hat{\alpha}_n^{(h-1)}, \hat{\alpha}_m^{(h-1)}) &= C - K \log \det [\mathbf{S}_{n,m} \\ &+ (\mathbf{z}_1 - \alpha_1 \mathbf{v}_R) (\mathbf{z}_1 - \alpha_1 \mathbf{v}_R)^\dagger + (\mathbf{Z}_{n,m} - \mathbf{V}_{SRS} \mathbf{A}_{n,m}^{(h-1)}) \\ &\times (\mathbf{Z}_{n,m} - \mathbf{V}_{SRS} \mathbf{A}_{n,m}^{(h-1)})^\dagger], \end{aligned} \quad (23)$$

where $C = KN \log[K/(\pi e)]$, $\mathbf{Z}_{n,m} = [\mathbf{z}_n, \mathbf{z}_m]$, $\mathbf{V}_{SRS} = [\mathbf{v}_{SR}, \mathbf{v}_S]$, and $\mathbf{A}_{n,m}^{(h-1)} = \text{diag}([\hat{\alpha}_n^{(h-1)}, \hat{\alpha}_m^{(h-1)}]^T)$. Now, let us define

$$\begin{aligned} \mathbf{C}_{n,m}^{(h-1)} &= \mathbf{S}_{n,m} + (\mathbf{Z}_{n,m} - \mathbf{V}_{SRS} \mathbf{A}_{n,m}^{(h-1)}) \\ &\times (\mathbf{Z}_{n,m} - \mathbf{V}_{SRS} \mathbf{A}_{n,m}^{(h-1)})^\dagger, \end{aligned} \quad (24)$$

then (23) can be recast as

$$\begin{aligned} C - K \log \det [\mathbf{C}_{n,m}^{(h-1)}] - K \\ \times \log [1 + (\mathbf{z}_1 - \alpha_1 \mathbf{v}_R)^\dagger (\mathbf{C}_{n,m}^{(h-1)})^{-1} (\mathbf{z}_1 - \alpha_1 \mathbf{v}_R)]. \end{aligned} \quad (25)$$

Maximizing the above function with respect to α_1 is tantamount to minimizing the argument of the logarithm, namely

$$\min_{\alpha_1} [(\mathbf{z}_1 - \alpha_1 \mathbf{v}_R)^\dagger (\mathbf{C}_{n,m}^{(h-1)})^{-1} (\mathbf{z}_1 - \alpha_1 \mathbf{v}_R)] \quad (26)$$

that is a well-known problem leading to

$$\hat{\alpha}_1^{(h)} = \frac{\mathbf{v}_R^\dagger (\mathbf{C}_{n,m}^{(h-1)})^{-1} \mathbf{z}_1}{\mathbf{v}_R^\dagger (\mathbf{C}_{n,m}^{(h-1)})^{-1} \mathbf{v}_R}. \quad (27)$$

Now, according to step 2, we consider

$$\begin{aligned} \log g(\hat{\alpha}_1^{(h)}, \alpha_n, \hat{\alpha}_m^{(h-1)}) &= C - K \log \det [\mathbf{S}_{n,m} \\ &+ (\mathbf{z}_n - \alpha_n \mathbf{v}_{SR}) (\mathbf{z}_n - \alpha_n \mathbf{v}_{SR})^\dagger + (\mathbf{Z}_{1,m} - \mathbf{V}_{RS} \mathbf{A}_{1,m}^{(h-1)}) \\ &\times (\mathbf{Z}_{1,m} - \mathbf{V}_{RS} \mathbf{A}_{1,m}^{(h-1)})^\dagger], \end{aligned} \quad (28)$$

where $\mathbf{V}_{RS} = [\mathbf{v}_R, \mathbf{v}_S]$, $\mathbf{A}_{1,m}^{(h-1)} = \text{diag}([\hat{\alpha}_1^{(h)}, \hat{\alpha}_m^{(h-1)}]^T)$, and $\mathbf{Z}_{1,m} = [\mathbf{z}_1, \mathbf{z}_m]$. Following the same line of reasoning as for α_1 , we come up with the following update for the estimate of α_n

$$\hat{\alpha}_n^{(h)} = \frac{\mathbf{v}_{SR}^\dagger (\mathbf{C}_{1,m}^{(h-1)})^{-1} \mathbf{z}_n}{\mathbf{v}_{SR}^\dagger (\mathbf{C}_{1,m}^{(h-1)})^{-1} \mathbf{v}_{SR}}, \quad (29)$$

where

$$\begin{aligned} \mathbf{C}_{1,m}^{(h-1)} &= \mathbf{S}_{n,m} + (\mathbf{Z}_{1,m} - \mathbf{V}_{RS} \mathbf{A}_{1,m}^{(h-1)}) \\ &\times (\mathbf{Z}_{1,m} - \mathbf{V}_{RS} \mathbf{A}_{1,m}^{(h-1)})^\dagger. \end{aligned} \quad (30)$$

Finally, we perform step 3 of the h th iteration by consid-

ering

$$\begin{aligned} \log g(\hat{\alpha}_1^{(h)}, \hat{\alpha}_n^{(h)}, \alpha_m) &= C - K \log \det [\mathbf{S}_{n,m}] \\ &+ (\mathbf{z}_m - \alpha_m \mathbf{v}_S) (\mathbf{z}_m - \alpha_m \mathbf{v}_S)^\dagger + \left(\mathbf{Z}_{1,n} - \mathbf{V}_{RSR} \mathbf{A}_{1,n}^{(h)} \right) \\ &\times \left(\mathbf{Z}_{1,n} - \mathbf{V}_{RSR} \mathbf{A}_{1,n}^{(h)} \right)^\dagger, \end{aligned} \quad (31)$$

where $\mathbf{Z}_{1,n} = [\mathbf{z}_1, \mathbf{z}_n]$, $\mathbf{A}_{1,n}^{(h)} = \text{diag}([\hat{\alpha}_1^{(h)}, \hat{\alpha}_n^{(h)}]^T)$, and $\mathbf{V}_{RSR} = [\mathbf{v}_R, \mathbf{v}_{SR}]$. It is not difficult to show that the optimization of the above function with respect to α_m leads to

$$\hat{\alpha}_m^{(h)} = \frac{\mathbf{v}_S^\dagger (\mathbf{C}_{1,n}^{(h)})^{-1} \mathbf{z}_n}{\mathbf{v}_S^\dagger (\mathbf{C}_{1,n}^{(h)})^{-1} \mathbf{v}_S}, \quad (32)$$

where

$$\begin{aligned} \mathbf{C}_{1,n}^{(h)} &= \mathbf{S}_{n,m} + \left(\mathbf{Z}_{1,n} - \mathbf{V}_{RSR} \mathbf{A}_{1,n}^{(h)} \right) \\ &\times \left(\mathbf{Z}_{1,n} - \mathbf{V}_{RSR} \mathbf{A}_{1,n}^{(h)} \right)^\dagger. \end{aligned} \quad (33)$$

Finally, denoting by \bar{h} the total number of iterations determined by the stopping criterion (see (22)), the cyclic GLRT (C-GLRT) is statistically equivalent to

$$\max_{\substack{n,m \in \Omega_P \\ n>1, m>n}} \frac{\det(\mathbf{S}_P + \mathbf{S}_S)}{\det [\mathbf{S}_{n,m} + \bar{\mathbf{Y}}_{1,n,m} \bar{\mathbf{Y}}_{1,n,m}^\dagger]} \begin{cases} H_1 & > \\ H_0 & \leq \end{cases} \eta, \quad (34)$$

where $\bar{\mathbf{Y}}_{1,n,m} = \mathbf{Z}_{1,n,m} - \mathbf{V} \hat{\mathbf{A}}$ and $\hat{\mathbf{A}} = \text{diag}([\hat{\alpha}_1^{(\bar{h})}, \hat{\alpha}_n^{(\bar{h})}, \hat{\alpha}_m^{(\bar{h})}]^T)$.

C. Approximate GLRT

The final approach consists in minimizing an upper bound to the objective function instead of the objective function itself. To be more definite, let us consider the following problem

$$\max_{\substack{n,m \in \Omega_P \\ n>1, m>n}} \max_{\boldsymbol{\alpha}} f(\mathbf{Z}_P, \mathbf{R}; \boldsymbol{\alpha}, n, m, \hat{\mathbf{M}}, H_1) \quad (35)$$

$$= \max_{\substack{n,m \in \Omega_P \\ n>1, m>n}} \max_{\boldsymbol{\alpha}} \left\{ \left[\frac{K}{\pi e} \right]^{KN} [\det(\mathbf{S}_{n,m} + \mathbf{Y}_{1,n,m})]^{-K} \right\} \quad (36)$$

and notice that the maximization with respect to $\boldsymbol{\alpha}$ requires to solve

$$\begin{aligned} &\min_{\boldsymbol{\alpha}} \det [\mathbf{S}_{n,m} + \mathbf{Y}_{1,n,m}] \\ &\Rightarrow \min_{\boldsymbol{\alpha}} \det [\mathbf{I} + (\mathbf{Z}_{1,n,m} - \mathbf{V} \mathbf{A})^\dagger \mathbf{S}_{n,m}^{-1} (\mathbf{Z}_{1,n,m} - \mathbf{V} \mathbf{A})] \\ &\Rightarrow \min_{\boldsymbol{\alpha}} \det [\mathbf{I} + (\mathbf{X}_{1,n,m} - \mathbf{V}_S \mathbf{A})^\dagger (\mathbf{X}_{1,n,m} - \mathbf{V}_S \mathbf{A})] \\ &\Rightarrow \min_{\boldsymbol{\alpha}} \det [\mathbf{I} + \mathbf{X}_{1,n,m}^\dagger \mathbf{X}_{1,n,m} \\ &+ ((\mathbf{V}_S^\dagger \mathbf{V}_S) \mathbf{A} - \mathbf{V}_S^\dagger \mathbf{X}_{1,n,m})^\dagger (\mathbf{V}_S^\dagger \mathbf{V}_S)^{-1} \\ &\times (\mathbf{V}_S^\dagger \mathbf{V}_S) \mathbf{A} - \mathbf{V}_S^\dagger \mathbf{X}_{1,n,m}] - \mathbf{X}_{1,n,m}^\dagger \mathbf{P}_{V_S} \mathbf{X}_{1,n,m} \\ &\Rightarrow \min_{\boldsymbol{\alpha}} \det [\mathbf{I} + \mathbf{X}_{1,n,m}^\dagger \mathbf{P}_{V_S}^\perp \mathbf{X}_{1,n,m} \\ &+ (\mathbf{B} \mathbf{A} - \mathbf{G}_{1,n,m})^\dagger (\mathbf{B} \mathbf{A} - \mathbf{G}_{1,n,m})], \end{aligned} \quad (37)$$

where¹⁰ $\mathbf{X}_{1,n,m} = \mathbf{S}_{n,m}^{-1/2} \mathbf{Z}_{1,n,m}$, $\mathbf{V}_S = \mathbf{S}_{n,m}^{-1/2} \mathbf{V}$, $\mathbf{P}_{V_S}^\perp = \mathbf{I} - \mathbf{V}_S (\mathbf{V}_S^\dagger \mathbf{V}_S)^{-1} \mathbf{V}_S^\dagger$, $\mathbf{B} = (\mathbf{V}_S^\dagger \mathbf{V}_S)^{1/2}$, and $\mathbf{G}_{1,n,m} = (\mathbf{V}_S^\dagger \mathbf{V}_S)^{-1/2} \mathbf{V}_S^\dagger \mathbf{X}_{1,n,m}$. If \mathbf{A} was a generic matrix, the minimizer would be

$$\tilde{\mathbf{A}} = \mathbf{B}^{-1} \mathbf{G}_{1,n,m} = (\mathbf{V}_S^\dagger \mathbf{V}_S)^{-1} \mathbf{V}_S^\dagger \mathbf{X}_{1,n,m}. \quad (38)$$

However, due to the structure of \mathbf{A} , the above estimate does not minimize the objective function in (37). Nevertheless, we resort to another approach to somehow solve (37). Specifically, since the logarithm is a monotone increasing function, the minimizer of the last problem is the same as that of the following problem

$$\min_{\boldsymbol{\alpha}} \log \det [\mathbf{I} + \mathbf{X}_{1,n,m}^\dagger \mathbf{P}_{V_S}^\perp \mathbf{X}_{1,n,m} + \mathbf{D}_{\boldsymbol{\alpha}}^{n,m}], \quad (39)$$

where $\mathbf{D}_{\boldsymbol{\alpha}}^{n,m} = (\mathbf{B} \mathbf{A} - \mathbf{G}_{1,n,m})^\dagger (\mathbf{B} \mathbf{A} - \mathbf{G}_{1,n,m})$. In addition, instead of minimizing the last objective function, we observe that for any positive definite matrix \mathbf{X} , the following inequality holds [43]

$$\log \det(\mathbf{X}) \leq \text{Tr}(\mathbf{X}) - N \quad (40)$$

and, hence,

$$\begin{aligned} &\min_{\boldsymbol{\alpha}} \log \det [\mathbf{I} + \mathbf{X}_{1,n,m}^\dagger \mathbf{P}_{V_S}^\perp \mathbf{X}_{1,n,m} + \mathbf{D}_{\boldsymbol{\alpha}}^{n,m}] \\ &\leq \min_{\boldsymbol{\alpha}} \left\{ \text{Tr} [\mathbf{I} + \mathbf{X}_{1,n,m}^\dagger \mathbf{P}_{V_S}^\perp \mathbf{X}_{1,n,m} + \mathbf{D}_{\boldsymbol{\alpha}}^{n,m}] - N \right\}. \end{aligned} \quad (41)$$

Therefore, we minimize the above upper bound with respect to $\boldsymbol{\alpha}$, namely

$$\min_{\boldsymbol{\alpha}} \text{Tr} [(\mathbf{B} \mathbf{A} - \mathbf{G}_{1,n,m})^\dagger (\mathbf{B} \mathbf{A} - \mathbf{G}_{1,n,m})] \quad (42)$$

$$\Rightarrow \min_{\boldsymbol{\alpha}} \|\mathbf{B} \mathbf{A} - \mathbf{G}_{1,n,m}\|_F^2. \quad (43)$$

Thus, we find an approximate solution by minimizing the Frobenius norm of $\mathbf{B} \mathbf{A} - \mathbf{G}_{1,n,m}$, that is

$$\begin{aligned} &\min_{\boldsymbol{\alpha}} \left[(\alpha_1 \mathbf{b}_1 - \mathbf{g}_1)^\dagger (\alpha_1 \mathbf{b}_1 - \mathbf{g}_1) + (\alpha_n \mathbf{b}_2 - \mathbf{g}_2)^\dagger \right. \\ &\quad \left. \times (\alpha_n \mathbf{b}_2 - \mathbf{g}_2) + (\alpha_m \mathbf{b}_3 - \mathbf{g}_3)^\dagger (\alpha_m \mathbf{b}_3 - \mathbf{g}_3) \right], \end{aligned} \quad (44)$$

where $\mathbf{B} = [\mathbf{b}_1, \mathbf{b}_2, \mathbf{b}_3]$ and $\mathbf{G}_{1,n,m} = [\mathbf{g}_1, \mathbf{g}_2, \mathbf{g}_3]$ (again, in order not to burden the notation we have omitted the dependence on n and m). Setting to zero the gradient of the above objective function, we come up with

$$\bar{\alpha}_1 = \frac{\mathbf{b}_1^\dagger \mathbf{g}_1}{\mathbf{b}_1^\dagger \mathbf{b}_1}, \quad \bar{\alpha}_n = \frac{\mathbf{b}_2^\dagger \mathbf{g}_2}{\mathbf{b}_2^\dagger \mathbf{b}_2}, \quad \bar{\alpha}_m = \frac{\mathbf{b}_3^\dagger \mathbf{g}_3}{\mathbf{b}_3^\dagger \mathbf{b}_3}. \quad (45)$$

Moreover, let us observe that

$$\left[\text{diag}([\mathbf{b}_1^\dagger \mathbf{b}_1, \mathbf{b}_2^\dagger \mathbf{b}_2, \mathbf{b}_3^\dagger \mathbf{b}_3]^T) \right]^{-1} \mathbf{B}^\dagger \mathbf{G}_{1,n,m}$$

¹⁰Notice that it is understood that \mathbf{V} is full-column rank.

$$\begin{aligned}
&= \begin{bmatrix} \mathbf{b}_1^\dagger \mathbf{g}_1 & \mathbf{b}_1^\dagger \mathbf{g}_2 & \mathbf{b}_1^\dagger \mathbf{g}_3 \\ \mathbf{b}_1^\dagger \mathbf{b}_1 & \mathbf{b}_1^\dagger \mathbf{b}_1 & \mathbf{b}_1^\dagger \mathbf{b}_1 \\ \mathbf{b}_2^\dagger \mathbf{g}_1 & \mathbf{b}_2^\dagger \mathbf{g}_2 & \mathbf{b}_2^\dagger \mathbf{g}_3 \\ \mathbf{b}_2^\dagger \mathbf{b}_2 & \mathbf{b}_2^\dagger \mathbf{b}_2 & \mathbf{b}_2^\dagger \mathbf{b}_2 \\ \mathbf{b}_3^\dagger \mathbf{g}_1 & \mathbf{b}_3^\dagger \mathbf{g}_2 & \mathbf{b}_3^\dagger \mathbf{g}_3 \\ \mathbf{b}_3^\dagger \mathbf{b}_3 & \mathbf{b}_3^\dagger \mathbf{b}_3 & \mathbf{b}_3^\dagger \mathbf{b}_3 \end{bmatrix} \\
&= \left[\text{diag}(\mathbf{V}_S^\dagger \mathbf{V}_S) \right]^{-1} \mathbf{V}_S^\dagger \mathbf{X}_{1,n,m} \quad (46)
\end{aligned}$$

and, hence, we obtain

$$\bar{\alpha}_1 = \frac{\mathbf{v}_R^\dagger \mathbf{S}_{n,m}^{-1} \mathbf{z}_1}{\mathbf{v}_R^\dagger \mathbf{S}_{n,m}^{-1} \mathbf{v}_R} = \hat{\alpha}_1(\mathbf{S}_{n,m}), \quad (47)$$

$$\bar{\alpha}_n = \frac{\mathbf{v}_{SR}^\dagger \mathbf{S}_{n,m}^{-1} \mathbf{z}_n}{\mathbf{v}_{SR}^\dagger \mathbf{S}_{n,m}^{-1} \mathbf{v}_{SR}} = \hat{\alpha}_n(\mathbf{S}_{n,m}), \quad (48)$$

$$\bar{\alpha}_m = \frac{\mathbf{v}_S^\dagger \mathbf{S}_{n,m}^{-1} \mathbf{z}_m}{\mathbf{v}_S^\dagger \mathbf{S}_{n,m}^{-1} \mathbf{v}_S} = \hat{\alpha}_m(\mathbf{S}_{n,m}). \quad (49)$$

Two remarks are now in order. First, the constraint on the rank of \mathbf{V} is no longer required. Second, observe that these solutions cannot be obtained by assigning to α_1 , α_n , and α_m the entries $\tilde{\mathbf{A}}(1,1)$, $\tilde{\mathbf{A}}(2,2)$, and $\tilde{\mathbf{A}}(3,3)$ given by (38), respectively. As a matter of fact, in (38), the term $\mathbf{V}_S^\dagger \mathbf{X}_{1,n,m}$ is multiplied (from the left) by the inverse of $\mathbf{V}_S^\dagger \mathbf{V}_S$ that is different from a diagonal matrix whose nonzero elements are the inverse of the terms in the principal diagonal of $\mathbf{V}_S^\dagger \mathbf{V}_S$.

The final expression of the decision rule is given by

$$\max_{\substack{n,m \in \Omega_P \\ n>1, m>n}} \frac{\det(\mathbf{S}_P + \mathbf{S}_S)}{\det[\mathbf{S}_{n,m} + \mathbf{Q}_{n,m}]} \frac{H_1}{H_0} \eta, \quad (50)$$

where $\mathbf{Q}_{n,m} = (\mathbf{Z}_{1,n,m} - \mathbf{V}\bar{\mathbf{A}})(\mathbf{Z}_{1,n,m} - \mathbf{V}\bar{\mathbf{A}})^\dagger$ and $\bar{\mathbf{A}} = \text{diag}([\bar{\alpha}_1, \bar{\alpha}_n, \bar{\alpha}_m]^T)$. The above decision scheme is referred to in the following as approximate GLRT (A-GLRT).

IV. On the CFAR Property

In this section, we investigate the CFAR behavior of the proposed decision schemes with respect to the unknown covariance matrix of the disturbance. To this end, we distinguish between the disturbance power and correlation by writing the covariance matrix as the product of a scaling factor $\gamma^2 > 0$ (representing the disturbance power) and a covariance structure $\mathbf{\Gamma} \in \mathbb{C}^{N \times N}$ (that depends on the disturbance correlation shape), i.e., $\mathbf{M} = \gamma^2 \mathbf{\Gamma}$.¹¹

Let us start from the EP-GLRT-KM-1 and write $\mathbf{z}_1 = \gamma \mathbf{w}_1$, $\mathbf{z}_i = \gamma \mathbf{w}_i$, $i = n, m$, and $\mathbf{r}_k = \gamma \mathbf{t}_k$, $k \in \Omega_S$. Under H_0 , for $i = n, m$ and $k \in \Omega_S$, $\mathbf{w}_1, \mathbf{w}_i, \mathbf{t}_k \sim \mathcal{CN}_N(\mathbf{0}, \mathbf{\Gamma})$.

¹¹In a clutter-dominated environment, the disturbance power coincides with the clutter power.

Then, the decision statistics can be written as

$$\begin{aligned}
&\max_{\substack{n,m \in \Omega_P \\ n>1, m>n}} \left\{ \frac{|\mathbf{v}_R^\dagger \mathbf{T}^{-1} \mathbf{w}_1|^2}{\mathbf{v}_R^\dagger \mathbf{T}^{-1} \mathbf{v}_R} + \frac{|\mathbf{v}_{SR}^\dagger \mathbf{T}^{-1} \mathbf{w}_n|^2}{\mathbf{v}_{SR}^\dagger \mathbf{T}^{-1} \mathbf{v}_{SR}} \right. \\
&\quad \left. + \frac{|\mathbf{v}_S^\dagger \mathbf{T}^{-1} \mathbf{w}_m|^2}{\mathbf{v}_S^\dagger \mathbf{T}^{-1} \mathbf{v}_S} \right\} \frac{H_1}{H_0} \eta, \quad (51)
\end{aligned}$$

where $\mathbf{T} = \sum_{k \in \Omega_S} \mathbf{t}_k \mathbf{t}_k^\dagger$, showing that it is invariant to data scaling operations. The same line of reasoning can be also used for EP-GLRT-KM-2, EP-GLRT-KA, and A-GLRT to show their invariance with respect to γ . Thus, we omit the steps of the proof except for the following key equalities that can be used for the proofs

$$\frac{\mathbf{v}_R^\dagger \mathbf{S}_S^{-1} \mathbf{z}_1}{\mathbf{v}_R^\dagger \mathbf{S}_S^{-1} \mathbf{v}_R} = \gamma \frac{\mathbf{v}_R^\dagger \mathbf{T}^{-1} \mathbf{w}_1}{\mathbf{v}_R^\dagger \mathbf{T}^{-1} \mathbf{v}_R}, \quad (52)$$

$$\frac{\mathbf{v}_{SR}^\dagger \mathbf{S}_S^{-1} \mathbf{z}_n}{\mathbf{v}_{SR}^\dagger \mathbf{S}_S^{-1} \mathbf{v}_{SR}} = \gamma \frac{\mathbf{v}_{SR}^\dagger \mathbf{T}^{-1} \mathbf{w}_n}{\mathbf{v}_{SR}^\dagger \mathbf{T}^{-1} \mathbf{v}_{SR}}, \quad (53)$$

$$\frac{\mathbf{v}_S^\dagger \mathbf{S}_S^{-1} \mathbf{z}_m}{\mathbf{v}_S^\dagger \mathbf{S}_S^{-1} \mathbf{v}_S} = \gamma \frac{\mathbf{v}_S^\dagger \mathbf{T}^{-1} \mathbf{w}_m}{\mathbf{v}_S^\dagger \mathbf{T}^{-1} \mathbf{v}_S}, \quad (54)$$

$$\frac{\mathbf{v}_R^\dagger \mathbf{S}_{n,m}^{-1} \mathbf{z}_1}{\mathbf{v}_R^\dagger \mathbf{S}_{n,m}^{-1} \mathbf{v}_R} = \gamma \frac{\mathbf{v}_R^\dagger \mathbf{T}_{n,m}^{-1} \mathbf{w}_1}{\mathbf{v}_R^\dagger \mathbf{T}_{n,m}^{-1} \mathbf{v}_R}, \quad (55)$$

$$\frac{\mathbf{v}_{SR}^\dagger \mathbf{S}_{n,m}^{-1} \mathbf{z}_n}{\mathbf{v}_{SR}^\dagger \mathbf{S}_{n,m}^{-1} \mathbf{v}_{SR}} = \gamma \frac{\mathbf{v}_{SR}^\dagger \mathbf{T}_{n,m}^{-1} \mathbf{w}_n}{\mathbf{v}_{SR}^\dagger \mathbf{T}_{n,m}^{-1} \mathbf{v}_{SR}}, \quad (56)$$

$$\frac{\mathbf{v}_S^\dagger \mathbf{S}_{n,m}^{-1} \mathbf{z}_m}{\mathbf{v}_S^\dagger \mathbf{S}_{n,m}^{-1} \mathbf{v}_S} = \gamma \frac{\mathbf{v}_S^\dagger \mathbf{T}_{n,m}^{-1} \mathbf{w}_m}{\mathbf{v}_S^\dagger \mathbf{T}_{n,m}^{-1} \mathbf{v}_S}, \quad (57)$$

where $\mathbf{T}_{n,m} = \mathbf{T} + \sum_{k \in \Omega_P \setminus \{1, n, m\}} \mathbf{w}_k \mathbf{w}_k^\dagger$.

As for the C-GLRT, the proof is more involved due to the cyclic estimation procedures and the CFAR behavior strictly depends on the initial values. Specifically, let us write

$$\alpha_n^{(h-1)} = \gamma u_n^{(h-1)}(\mathcal{D}), \quad \alpha_m^{(h-1)} = \gamma u_m^{(h-1)}(\mathcal{D}) \quad (58)$$

where $\mathcal{D} = \{\mathbf{x}_1, \dots, \mathbf{x}_{K_P}, \mathbf{t}_1, \dots, \mathbf{t}_{K_S}\}$, then, we can write

$$\begin{aligned}
\mathbf{C}_{n,m}^{(h-1)} &= \gamma^2 \mathbf{T}_{n,m} + \gamma^2 \left(\mathbf{W}_{n,m} - \mathbf{V}_{SRS} \mathbf{U}_{n,m}^{(h-1)} \right) \\
&\quad \times \left(\mathbf{W}_{n,m} - \mathbf{V}_{SRS} \mathbf{U}_{n,m}^{(h-1)} \right)^\dagger \\
&= \gamma^2 \tilde{\mathbf{C}}_{n,m}^{(h-1)},
\end{aligned} \quad (59)$$

where $\mathbf{W}_{n,m} = [\mathbf{w}_n, \mathbf{w}_m] \in \mathbb{C}^{N \times 2}$, the expression of $\tilde{\mathbf{C}}_{n,m}^{(h-1)}$ can be easily obtained from the above equation, and $\mathbf{U}_{n,m}^{(h-1)} = \text{diag}([u_n^{(h-1)}(\mathbf{W}), u_m^{(h-1)}(\mathbf{W})]^T) \in \mathbb{C}^{2 \times 2}$. As a consequence, the update equation for α_1 (step 1) can be recast as

$$\hat{\alpha}_1^{(h)} = \gamma \frac{\mathbf{v}_R^\dagger (\tilde{\mathbf{C}}_{n,m}^{(h-1)})^{-1} \mathbf{w}_1}{\mathbf{v}_R^\dagger (\tilde{\mathbf{C}}_{n,m}^{(h-1)})^{-1} \mathbf{v}_R} = \gamma u_1^{(h)}(\mathcal{D}). \quad (60)$$

Focusing on step 2 of the h th iteration, we observe that

$$\begin{aligned} \mathbf{C}_{1,m}^{(h-1)} &= \gamma^2 \mathbf{T}_{n,m} + \gamma^2 \left(\mathbf{W}_{1,m} - \mathbf{V}_{RS} \mathbf{U}_{1,m}^{(h-1)} \right) \\ &\quad \times \left(\mathbf{W}_{1,m} - \mathbf{V}_{RS} \mathbf{U}_{1,m}^{(h-1)} \right)^\dagger \\ &= \gamma^2 \tilde{\mathbf{C}}_{1,m}^{(h-1)}, \end{aligned} \quad (61)$$

where $\mathbf{W}_{1,m} = [\mathbf{w}_1, \mathbf{w}_m] \in \mathbb{C}^{N \times 2}$ and $\mathbf{U}_{1,m}^{(h-1)} = \text{diag}([u_1^{(h)}(\mathcal{D}), u_m^{(h-1)}(\mathcal{D})]^T) \in \mathbb{C}^{2 \times 2}$, and, hence, the estimate of α_n can be written as

$$\hat{\alpha}_n^{(h)} = \gamma \frac{\mathbf{v}_{SR}^\dagger (\tilde{\mathbf{C}}_{1,m}^{(h-1)})^{-1} \mathbf{w}_n}{\mathbf{v}_{SR}^\dagger (\tilde{\mathbf{C}}_{1,m}^{(h-1)})^{-1} \mathbf{v}_{SR}} = \gamma u_n^{(h)}(\mathcal{D}). \quad (62)$$

Finally, we apply the same line of reasoning to step 3. Thus, we can write

$$\begin{aligned} \mathbf{C}_{1,n}^{(h)} &= \gamma^2 \mathbf{T}_{n,m} + \gamma^2 \left(\mathbf{W}_{1,n} - \mathbf{V}_{RSR} \mathbf{U}_{1,n}^{(h)} \right) \\ &\quad \times \left(\mathbf{W}_{1,n} - \mathbf{V}_{RSR} \mathbf{U}_{1,n}^{(h)} \right)^\dagger \\ &= \gamma^2 \tilde{\mathbf{C}}_{1,n}^{(h)}, \end{aligned} \quad (63)$$

where $\mathbf{W}_{1,n} = [\mathbf{w}_1, \mathbf{w}_n] \in \mathbb{C}^{N \times 2}$ and $\mathbf{U}_{1,n}^{(h)} = \text{diag}([u_1^{(h)}(\mathcal{D}), u_n^{(h)}(\mathcal{D})]^T) \in \mathbb{C}^{2 \times 2}$. Then, the estimate of α_m can be recast as

$$\hat{\alpha}_m^{(h)} = \gamma \frac{\mathbf{v}_S^\dagger (\tilde{\mathbf{C}}_{1,n}^{(h)})^{-1} \mathbf{w}_m}{\mathbf{v}_S^\dagger (\tilde{\mathbf{C}}_{1,n}^{(h)})^{-1} \mathbf{v}_S} = \gamma u_m^{(h)}(\mathcal{D}). \quad (64)$$

At the end of the iterative procedure, it is possible to show that the left-hand side of (34) is functionally independent of γ . Thus, if (58) holds for $h = 1$, then the C-GLRT is invariant to the clutter power.

Now, let us focus on the structure $\mathbf{\Gamma}$ and notice that proving the invariance with respect to $\mathbf{\Gamma}$ (at least to the best of authors' knowledge) is not an easy task due to the joint presence of different steering vectors in the decision statistics. Nevertheless, we show below that all the decision schemes are bounded CFAR meaning that they are limited from above by a statistic that is invariant with respect to \mathbf{M} (and, hence, $\mathbf{\Gamma}$). As a matter of fact, starting from the estimates and plug solutions, $\forall n, m \in \Omega_P$ the following inequality holds

$$\begin{aligned} \frac{|\mathbf{v}_R^\dagger \mathbf{S}_S^{-1} \mathbf{z}_1|^2}{\mathbf{v}_R^\dagger \mathbf{S}_S^{-1} \mathbf{v}_R} + \frac{|\mathbf{v}_{SR}^\dagger \mathbf{S}_S^{-1} \mathbf{z}_n|^2}{\mathbf{v}_{SR}^\dagger \mathbf{S}_S^{-1} \mathbf{v}_{SR}} + \frac{|\mathbf{v}_S^\dagger \mathbf{S}_S^{-1} \mathbf{z}_m|^2}{\mathbf{v}_S^\dagger \mathbf{S}_S^{-1} \mathbf{v}_S} \\ \leq \mathbf{z}_1^\dagger \mathbf{S}_S^{-1} \mathbf{z}_1 + \sum_{i=n,m} \mathbf{z}_i^\dagger \mathbf{S}_S^{-1} \mathbf{z}_i \end{aligned} \quad (65)$$

and, hence, we have that

$$\begin{aligned} \max_{n,m \in \Omega_P} \left\{ \frac{|\mathbf{v}_R^\dagger \mathbf{S}_S^{-1} \mathbf{z}_1|^2}{\mathbf{v}_R^\dagger \mathbf{S}_S^{-1} \mathbf{v}_R} + \frac{|\mathbf{v}_{SR}^\dagger \mathbf{S}_S^{-1} \mathbf{z}_n|^2}{\mathbf{v}_{SR}^\dagger \mathbf{S}_S^{-1} \mathbf{v}_{SR}} + \frac{|\mathbf{v}_S^\dagger \mathbf{S}_S^{-1} \mathbf{z}_m|^2}{\mathbf{v}_S^\dagger \mathbf{S}_S^{-1} \mathbf{v}_S} \right\} \\ \leq \max_{n,m \in \Omega_P} \left\{ \mathbf{z}_1^\dagger \mathbf{S}_S^{-1} \mathbf{z}_1 + \sum_{i=n,m} \mathbf{z}_i^\dagger \mathbf{S}_S^{-1} \mathbf{z}_i \right\}. \end{aligned} \quad (66)$$

Now, notice that the statistical characterization of

$\mathbf{z}_l^\dagger \mathbf{S}_S^{-1} \mathbf{z}_l$, $l \in \{1, n, m\}$, under H_0 , does not depend on \mathbf{M} . In fact it can be written as $\mathbf{z}_{l,0}^\dagger \mathbf{S}_{S,0}^{-1} \mathbf{z}_{l,0}$, where $\mathbf{z}_{l,0} = \mathbf{M}^{-1/2} \mathbf{z}_l \sim \mathcal{CN}_N(\mathbf{0}, \mathbf{I})$ and $\mathbf{S}_{S,0} = \mathbf{M}^{-1/2} \mathbf{S}_S \mathbf{M}^{-1/2} \sim \mathcal{CW}_N(K_S, \mathbf{I})$ are random quantities independent of \mathbf{M} . It follows that the right-hand side of (66) under H_0 is invariant with respect to \mathbf{M} (and, hence, to $\mathbf{\Gamma}$). This property can be similarly proved also for the EP-GLRT-KM-2 when \mathbf{S}_S is replaced by $\mathbf{S}_{n,m}$.

As for the EP-GLRT-KA (18), the C-GLRT (34), and the A-GLRT (50), we exploit the inequality [43]

$$\det(\mathbf{A} + \mathbf{B}) \geq \det(\mathbf{A}), \quad (67)$$

where $\mathbf{A} \in \mathbb{C}^{N \times N}$ is positive definite and $\mathbf{B} \in \mathbb{C}^{N \times N}$ is positive semidefinite, to obtain

$$\left. \begin{aligned} \max_{\substack{n,m \in \Omega_P \\ n > 1, m > n}} \frac{\det(\mathbf{S}_P + \mathbf{S}_S)}{\det[\mathbf{S}_{n,m} + \mathbf{Y}_{1,n,m}]} \\ \max_{\substack{n \in \Omega_P \\ n > 1, m > n}} \frac{\det(\mathbf{S}_P + \mathbf{S}_S)}{\det(\mathbf{S}_{n,m} + \bar{\mathbf{Y}}_{1,n,m})} \\ \max_{\substack{n,m \in \Omega_P \\ n > 1, m > n}} \frac{\det(\mathbf{S}_P + \mathbf{S}_S)}{\det[\mathbf{S}_{n,m} + \mathbf{Q}_{n,m}]} \end{aligned} \right\} \leq \max_{\substack{n,m \in \Omega_P \\ n > 1, m > n}} \frac{\det(\mathbf{S}_P + \mathbf{S}_S)}{\det[\mathbf{S}_{n,m}]} \quad (68)$$

Now, the right-hand side of the previous equation can be recast as

$$\begin{aligned} \max_{\substack{n,m \in \Omega_P \\ n > 1, m > n}} \frac{\det(\mathbf{S}_{P,0} + \mathbf{S}_{S,0}) \det(\mathbf{M})}{\det[\mathbf{S}_{n,m,0}] \det(\mathbf{M})} \\ = \max_{\substack{n,m \in \Omega_P \\ n > 1, m > n}} \frac{\det(\mathbf{S}_{P,0} + \mathbf{S}_{S,0})}{\det[\mathbf{S}_{n,m,0}]}, \end{aligned} \quad (69)$$

where $\mathbf{S}_{P,0} = \sum_{k=1}^{K_P} \mathbf{M}^{-1/2} \mathbf{z}_k \mathbf{z}_k^\dagger \mathbf{M}^{-1/2}$ and $\mathbf{S}_{n,m,0} = \mathbf{M}^{-1/2} \mathbf{S}_{n,m} \mathbf{M}^{-1/2} \sim \mathcal{CW}_N(K_S + K_P - 3, \mathbf{I})$. Again, neither the statistical characterization of $\mathbf{S}_{P,0}$, $\mathbf{S}_{n,m,0}$, and $\mathbf{S}_{S,0}$ or their correlation depend on \mathbf{M} and, hence, the right-hand side of the last equation is invariant with respect to \mathbf{M} .

V. RCS of Low-RCS Aircrafts and RIS Design Issues

The purpose of this section is twofold. First, we start with the description of the main design principles used to reduce the RCS of an aircraft also providing examples of practical value. Then, we proceed by indicating some guidelines to develop a RIS tailored for the specific application.

A. Low-RCS Aircrafts: Examples

The RCS of an aircraft is not a single number but a complex signature dictated by four fundamental pillars. Shape is the paramount factor, where specific geometries are designed to deflect radar waves away from the source. Materials play a crucial supporting role, with radar-absorbing materials (RAM) converting incident radar energy into heat to reduce reflection. Intrinsic reflectivity involves managing the inherent properties of surfaces and, critically, concealing cavity reflectors like engine inlets and

cockpits, which are major sources of radar returns. Finally, aspect angle acknowledges that an aircraft's RCS is highly dynamic, leading designers to strategically optimize stealth for a specific "threat sector," most commonly the frontal aspect, accepting higher signatures from less critical angles.

The practical application of RCS reduction principles can be best understood by examining iconic stealth aircraft, each representing a different evolutionary stage and design philosophy. The evolution of stealth aircraft demonstrates a progression in design philosophy and technology. The F-117 Nighthawk pioneered operational stealth by using faceted geometry to deflect radar waves in specific directions, a calculable but aerodynamically inefficient method effective from frontal angles. The B-2 Spirit represented a major advance with its flying-wing shape and continuous curves, creating an all-aspect stealth design that scatters radar energy weakly and provides a consistently low signature from any direction. Finally, the F-22 Raptor and F-35 Lightning II synthesize stealth with high performance. They use a blend of planform alignment and curved surfaces, heavily optimized for a low frontal RCS for air dominance. Key features include internal weapon bays and concealed engine inlets, with the F-35 incorporating advanced materials for better sustainability. The F-35 is designed to significantly reduce radar returns, particularly in the X-band frequency range, where most fire-control and targeting radars operate [44]–[48]. These measures are most effective in the frontal hemisphere, where the aircraft presents minimal surface discontinuities and optimized planform alignment, resulting in an RCS as low as -40 dBsm under ideal nose-on conditions [49]. In Table I, we show the estimated RCS values for dim airborne targets that fly at a low altitude of 500 meters and is viewed from a range of 40 km; the radar sees the aircraft at an elevation angle of approximately 0.72° , revealing only its nose. This represents the stealth-optimal geometry, yielding an estimated RCS below -30 dBsm.

However, as the distance to the radar decreases, the elevation angle increases, exposing less stealth-optimized features on the lower fuselage, including the weapons bay doors, landing gear covers, and the trailing edges near the engine nozzle. At 10 km, the elevation angle increases to approximately 2.86° , and the estimated RCS rises to about -20 dBsm. When the range decreases further to 5 km, with an elevation angle of 5.71° , the radar has a clearer line of sight to the aircraft underbody, resulting in a further increase in RCS to the range $[-15, -20]$ dBsm. These values, while still significantly lower than those of conventional fourth-generation fighters (which typically exhibit RCS values between 1 and 5 m^2 in frontal aspects), demonstrate how even small shifts in viewing geometry can affect the radar observability of a stealth platform [33].

B. Case Study, Energy Considerations, and RIS Design

The investigated scenario is depicted in Figure 3. Specifically, given the reference system in the figure, the

positions of the radar system, the RIS, and the target are the following

- radar location: $(-30000, 200)$ m;
- RIS location: $(0, 0)$ m;
- target location: $(1000, 500)$ m.

In this context, the relevant distances are

$$\begin{cases} d_{RT} = \sqrt{31^2 + 0.3^2} \approx 31 \text{ km}, \\ d_{RS} = \sqrt{30^2 + 0.2^2} \approx 30 \text{ km}, \\ d_{ST} = \sqrt{1^2 + 0.5^2} \approx 1.2 \text{ km}, \end{cases} \quad (70)$$

and, assuming a range resolution of 20 m, it is not difficult to verify that the above values satisfy conditions (2). Based on the above parameters and distances, we can compute the incident and reflection angles relative to the RIS, which is placed at the origin of the reference system. The angle θ_{Si} is measured between the incoming wave (from radar to RIS) and the RIS normal (vertical axis) and is given by

$$\theta_{Si} = \tan^{-1} \left(\frac{30000}{200} \right) \approx 89.62^\circ. \quad (71)$$

The angle θ_{So} between the RIS-to-target line and the x -axis is

$$\theta_{So} = 90^\circ - \tan^{-1} \left(\frac{1000}{500} \right) \approx 26.5^\circ. \quad (72)$$

The simulation results shown in the next section assume that the carrier frequency of the radar is $f_c = 3$ GHz which corresponds to a wavelength of 10 cm. Moreover, the transmitted power is $P_T = 10$ kW and the transmit gain is $G_T = 37$ dBi, which means an effective area of the transmitting/receiving antenna being [50]

$$A_{eff} = \frac{\lambda^2 G_T}{4\pi}. \quad (73)$$

In order to compute the received energy according to the different paths, we need to know the values of the target monostatic and bistatic RCSs. Specifically, the target RCS values considered are

- LOS path: $\sigma_{RTR} = 10^{-2} \text{ m}^2$ (i.e., -20 dBsm);
- RIS-RIS path: $\sigma_{STS} = 1 \text{ m}^2$ (i.e., 0 dBsm);
- RIS-assisted LOS: $\sigma_{STR} = 1 \text{ m}^2$ (i.e., 0 dBsm).

Thus, the received power for the different paths as a function of the RIS RCS is

- LOS path:

$$P_R^{RTR}(\sigma_{RIS}) = \frac{P_T G_T \sigma_{RTR} A_{eff}}{(4\pi)^2 d_{RT}^4}; \quad (74)$$

- RIS-assisted LOS Path (single bounce):

$$\begin{aligned} P_R^{RSTR}(\sigma_{RIS}) &= \frac{P_T G_T}{4\pi d_{RS}^2} \\ &\times \sigma_{RIS} \frac{1}{4\pi d_{ST}^2} \sigma_{STR} \frac{A_{eff}}{4\pi d_{RT}^2}; \end{aligned} \quad (75)$$

TABLE I: Monostatic and bistatic RCS estimates for low-RCS aircrafts in S-band (2-4 GHz)

Case	Geometry	Estimated RCS	Notes
RTR (radar-target-radar)	Monostatic, nose-on ($\theta_i \approx 0^\circ$)	-30 dBsm to -20 dBsm	Best-case stealth performance.
STS (surface-target-surface)	Monostatic, $\theta_{So} \approx 30^\circ$ off-nose	-10 dBsm to 0 dBsm	Monostatic from RIS
RTS (radar-target-surface)	Bistatic ($\theta_{So} \approx 30^\circ$), Rx at nose ($\theta_i \approx 0^\circ$)	-10 dBsm to 0 dBsm	Bistatic path

Additional notes:

- All values assume clean aircraft configuration (no weapons/doors open)
- Bistatic advantage is less pronounced in S-band than X-band but still measurable
- Worst-case side aspect (90°) could reach -5 dBsm to 10 dBsm in S-band

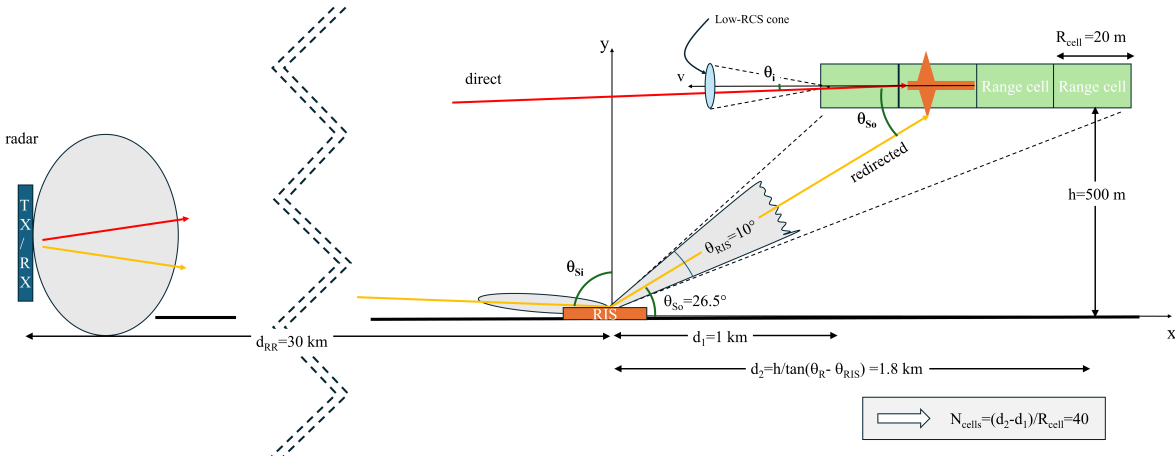


Fig. 3: Geometry of the investigated operating scenario.

- RIS-RIS Path (double bounce):

$$P_R^{RSTS R}(\sigma_{RIS}) = \frac{P_T G_T}{(4\pi d_{RS}^2)^2} \times \sigma_{RIS}^2 \frac{1}{(4\pi d_{ST}^2)^2} \sigma_{STS} A_{eff}. \quad (76)$$

In Figure 4, we plot the ratio of the received power over transmitted power as a function of the RIS RCS σ_{RIS} , which sweeps from 10 dBsm to 70 dBsm, for the three paths by using the aforementioned parameter values. The curve obtained from (74) is constant as it does not depend on σ_{RIS} . The curves obtained from (75) and (76) indicate that in order to have a relevant contribution from secondary paths, the RIS should be designed with an RCS larger than 55 dBsm.

Now, we have all the elements to proceed with the design of the RIS. As a matter of fact, the above analysis draws some guidelines for the design of the RIS and, in particular, allows us to establish the minimum RIS aperture L_{RIS} such that the RIS-assisted path dominates the LOS path. To this end, we model the RIS as a square aperture of size $L_{RIS} \times L_{RIS}$. It is important to underline that a key advantage of a RIS (or, more generally, a metasurface) is its ability to control the aperture illumination profile, or tapering, either passively or actively. By manipulating the phase and amplitude of each unit cell, the reflected wavefront can be shaped to realize a desired tapering across the aperture, which directly impacts the effective RCS, beamwidth, and sidelobe levels.

Once an optimal phase or tapering profile is deter-

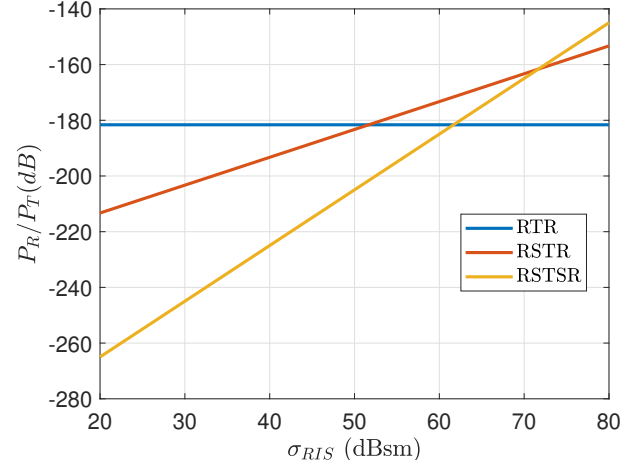


Fig. 4: Received power as a function of the RIS RCS for the three analyzed contributions.

mined (e.g., to steer reflected energy toward a target at a desired bistatic angle) the RIS configuration can be synthesized using a local periodicity approximation, a standard method in reflectarray antenna design [51], [52]. This approach allows the aperture illumination (tapering) to be tailored precisely, either statically or dynamically, providing agile control over beam shaping and effective RCS for stealthy or multi-angle observable targets.

The RIS can be also designed as reconfigurable surface. Active control is typically achieved using tunable elements such as varactors [5], [53], PIN diodes [54], or liquid

crystals [55]. Varactor diodes are especially attractive for radar RIS applications due to their continuous phase tuning, low power requirements, and high-speed response, enabling rapid adaptation to dynamic scenes. However, they require more complex analog biasing networks. PIN diodes simplify the circuitry as binary switches but offer coarse phase resolution. Liquid crystal-based RIS are promising for large-area and mm-wave applications, though their slower switching speed limits real-time radar use.

At the design stage, three illumination functions are considered along the x -axis: uniform illumination, sinc tapering, and linear frequency modulated (LFM) phase-only tapering (with uniform distribution along y). While uniform illumination maximizes the RIS RCS, it does not provide control over the beamwidth, which becomes increasingly narrow as the RIS size grows. This narrow beam is not compatible with the simultaneous illumination of multiple range cells. To address this, sinc and LFM tapering are investigated along the x -axis to achieve a controlled beamwidth over a predefined angular sector, allowing the designer to distribute energy across multiple targets or observation directions while maintaining an acceptable loss in terms of RIS RCS.

1) 2-dimensional Uniform Illumination: Considering a square surface with side length L_{RIS} , it is possible to show that the boresight RCS is:

$$\sigma_{\text{uniform}} = \frac{4\pi L_{\text{RIS}}^4}{\lambda^2}. \quad (77)$$

This corresponds to the maximum RCS achievable for a perfectly phased square aperture. This implies that the minimum RIS size that allows to get a relevant contribution from secondary paths is

$$L_{\text{RIS}} = \left(\frac{\sigma_{\text{RIS}} \lambda^2}{4\pi} \right)^{1/4} \quad (78)$$

Normalizing L_{RIS} with respect to wavelength, and assuming a periodicity of half-wavelength for the RIS elements, we get the number of elements per line, N_{RIS} :

$$N_{\text{RIS}} = \left\lceil 2 \frac{L_{\text{RIS}}}{\lambda} \right\rceil. \quad (79)$$

The Half Power Beamwidth (HPBW) of a uniform linear RIS array can then be approximated as [50]:

$$\text{HPBW} \approx \frac{2 \times 50.8^\circ}{N_{\text{RIS}}}, \quad (80)$$

which provides an estimate of the spatial resolution achievable with the RIS. By employing the design parameters, a HPBW angle of 1.5° is obtained. However, since a larger angle is needed to illuminate multiple radar cells (e.g., 10°) a sinc tapering of the surface can be employed.

2) Sinc Tapering along the x-axis and Uniform Illumination along y-axis: The surface current distribution imposed by the RIS can be written as

$$J_s(x, y) = 2 \frac{E_0}{\zeta_0} \text{sinc}\left(\frac{x}{b}\right) \text{rect}\left(\frac{x}{L_{\text{RIS}}}\right) \text{rect}\left(\frac{y}{L_{\text{RIS}}}\right), \quad (81)$$

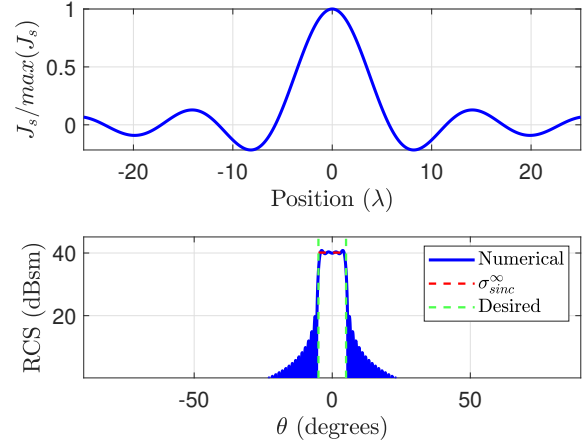


Fig. 5: Sinc tapering of the aperture and RCS pattern obtained for an aperture of 50λ .

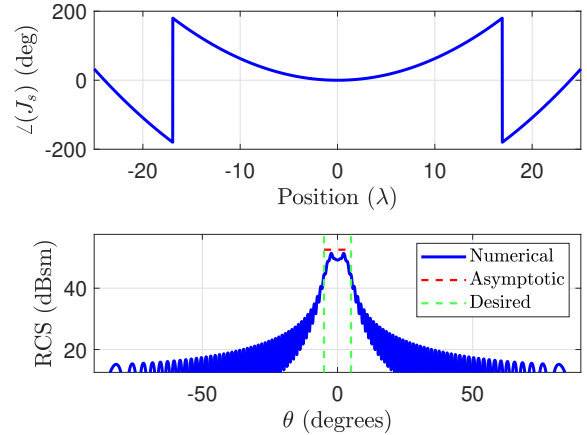


Fig. 6: LFM phase-only tapering of the aperture and RCS pattern obtained for an aperture of 50λ .

where E_0 is the impinging electric field, $\zeta_0 = \sqrt{\mu_0/\epsilon_0}$ is the free space impedance, where ϵ_0 and μ_0 represent the vacuum dielectric permittivity and permeability, respectively. The parameter b represents the mainlobe width and sidelobes' level; its definition is $b = \lambda/\phi_0$, where ϕ_0 is the desired beamwidth. An example is shown in Figure 5 where a sinc tapering is applied to an aperture of 50 wavelengths and a rectangular pattern with the desired beamwidth (10°) is obtained. The beamwidth control is paid in terms of maximum RCS of the aperture as corroborated by Figure 7.

At boresight, the RCS of the sinc-tapered aperture becomes:

$$\sigma_{\text{sinc}} = \frac{16b^2 L_{\text{RIS}}^2}{\pi \lambda^2} \text{Si}^2\left(\frac{\pi L_{\text{RIS}}}{2b}\right), \quad (82)$$

with $\text{Si}(z) = \int_0^z \frac{\sin t}{t} dt$. For a very large aperture ($L_{\text{RIS}} \rightarrow \infty$):

$$\sigma_{\text{sinc}}^{\infty} = \frac{4\pi b^2 L_{\text{RIS}}^2}{\lambda^2}. \quad (83)$$

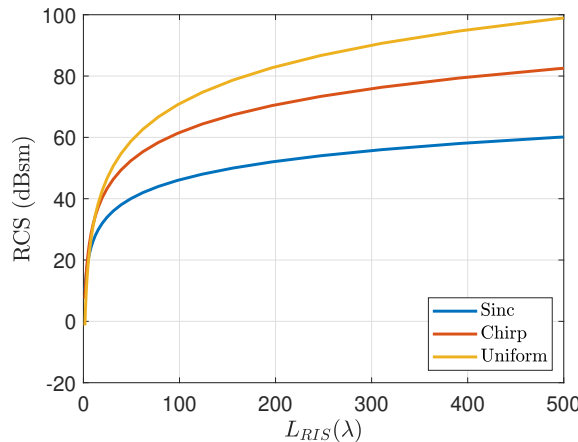


Fig. 7: Predicted RCS of a RIS with uniform and Sinc and LFM tapering for $\phi_0 = 10^\circ$.

3) LFM Phase-only Tapering along the x-axis and Uniform Illumination along y-axis: In case of LFM tapering [56], the RCS reduction is less critical than Sinc tapering and an acceptable beam control is allowed. An LFM-tapered RIS can be modeled by imposing a quadratic phase distribution along the x -axis, while maintaining uniform illumination along y . The resulting surface current density can be written as

$$J_s(x, y) = 2 \frac{E_0}{\zeta_0} e^{j\pi K_x x^2} \text{rect}\left(\frac{x}{L_{\text{RIS}}}\right) \text{rect}\left(\frac{y}{L_{\text{RIS}}}\right), \quad (84)$$

where K_x is the chirp rate that controls the angular spreading of the scattered field. In particular, for a rectangular beam of angular width ϕ_0 in the x - z plane, the chirp rate can be approximated as

$$K_x \simeq \frac{\phi_0}{\lambda L_{\text{RIS}}}, \quad (85)$$

which directly links the phase curvature to the desired beamwidth. The quadratic phase prevents coherent addition over the full aperture and limits the effective contributing region along the x -axis to a stationary-phase length, thereby redistributing the scattered energy over a broader angular sector, as illustrated in Figure 6. At boresight, the RCS of the LFM-tapered aperture can be asymptotically estimated using the stationary-phase method as

$$\sigma_{\text{chirp}}^\infty \approx \frac{4\pi}{\lambda^2} \left(L_{\text{RIS}} \sqrt{\frac{2}{K_x}} \right)^2 = \frac{8\pi}{\lambda^2} \frac{L_{\text{RIS}}^2}{K_x}. \quad (86)$$

Thus, for a very large aperture, the peak RCS scales linearly with the aperture dimension along the LFM-tapered direction, highlighting the fundamental tradeoff between angular beamwidth control and maximum achievable RCS in LFM-tapered RIS apertures.

The comparison of the RIS RCSs corresponding to the aforementioned tapering approaches is reported in Figure 7. The following concluding remarks can be drawn

- the uniform illumination maximizes the RCS, which

scales as L_{RIS}^4 but it does not provide any beamwidth control;

- Sinc tapering effectively reduces the coherent aperture along the x -direction, resulting in a lower peak RCS while enabling improved beam shaping and sidelobe suppression; the tapering parameter b controls the mainlobe width and the effective RCS: smaller values of b lead to wider beams at the expense of reduced peak RCS;
- LFM phase-only tapering represents an attractive compromise: although sidelobe control is suboptimal compared to amplitude tapering, it enables high RCS levels (exceeding 60 dBsm for a side length of 100λ) while providing flexible angular beam shaping through phase-only modulation.

VI. Performance Assessment

In this section, we assess the performance of the proposed detection schemes by generating target echoes according to the scenario described in Subsection V-B. The performance metric is the P_d (for a preassigned value of the P_{fa}) as a function of the SINR for the monostatic path (RTR) defined as

$$\text{SINR}_{\text{RTR}} = |\alpha_1|^2 \mathbf{v}_R \mathbf{M}^{-1} \mathbf{v}_R. \quad (87)$$

The above metric is estimated by resorting to standard Monte Carlo (MC) counting techniques. Specifically, we compute the detection thresholds and the P_d values over $100/P_{fa}$ and 10^4 independent trials, respectively. As for the radar system, we consider a uniform linear array formed by N vertically aligned sensors, whose inter-element spacing is equal to $\lambda/2$ with λ the operating wavelength and assume that only spatial processing is performed (for simplicity). The corresponding steering vector can be expressed as $\mathbf{v}(\theta) = [1, e^{j\pi \sin \theta}, \dots, e^{j\pi(N-1) \sin \theta}]^T \in \mathbb{C}^{N \times 1}$, where θ is the elevation angle. Based on Figure 3, we set $\theta = 0.5^\circ$ for \mathbf{v}_R and $\theta = -0.4^\circ$ for \mathbf{v}_S ; moreover, since only spatial channels are considered in the simulation setup, it follows that $\mathbf{v}_{S,1} = \mathbf{v}_S$ and $\mathbf{v}_{R,1} = \mathbf{v}_R$.

According to the design guidelines defined in the previous section, we consider LFM phase-only beamforming and a RIS whose size allows the bistatic paths to yield echoes with powers that are about 20 dB stronger than those from the monostatic path. Thus, once α_1 is set according to (87), we consider $\alpha_n = \alpha_m = 10\alpha_1$. Moreover, let us recall that the range resolution is 20 m and assume that the region under surveillance is formed by 20 out of 40 available range bins as indicated in Figure 3. Thus, exploiting the distances mentioned in Subsection V-B and assuming, for simplicity, that the monostatic echo occupies the first range bin, it is possible to show that the range bins containing the returns from the bistatic paths are indexed by $n = 3$ for the path RTSR (or RSTR) and $m = 6$ for the path RSTSR. With these values in mind,

we set $K_P = 6^{.12}$

As for the interference component, it is modeled as a complex Gaussian random vector with covariance matrix $\mathbf{M} = \sigma_n^2 \mathbf{I} + \mathbf{M}_c$, where $\sigma_n^2 = 1$ is the noise power and \mathbf{M}_c is the clutter covariance matrix whose (n, m) th entry is $\sigma_c^2 \rho^{|n-m|}$ with $\rho = 0.9$ the one-lag correlation coefficient and $\sigma_c^2 > 0$ the clutter power set according to the clutter-to-noise ratio (CNR) defined as $\text{CNR} = 10 \log_{10}(\sigma_c^2 / \sigma_n^2) = 25$ dB. Finally, in the following numerical examples, we assume $N = 16$ and $P_{fa} = 10^{-4}$.

A. Convergence of the C-GLRT

This subsection verifies the convergence rate of the C-GLRT algorithm. To this end, in Figure 8 we plot the left-hand side of (22), namely the relative variation of the function $g(\cdot)$ defined in Subsection III-B, averaged over 1000 MC trials versus the iteration index h and under H_1 when the target geometry generates different (n, m) pairs. In the numerical example, the training sample size is $K_S = 24, 32$. The figure shows that all the curves drop to very low values after some iteration. As a matter of fact, in (22), if we set $\epsilon = 10^{-5}$, the inequality is generally satisfied for $h \leq 8$. For this reason, in what follows, we use the above value for ϵ and we set $h_{\max} = 20$.

B. CFAR Property

In this subsection, we investigate the CFAR behavior of the proposed decision schemes with respect to variations of both the clutter power (i.e., σ_c^2) and the clutter correlation (i.e., ρ). To this end, we estimate the actual P_{fa} for the considered values of CNR or ρ when the used threshold corresponds to a nominal $P_{fa} = 10^{-4}$ obtained by setting CNR = 25 dB and $\rho = 0.9$. These estimates are computed with a training sample size $K_S = 24$. Figure 9a shows the variation of the estimated P_{fa} versus CNR (from -15 dB to 30 dB) when $\rho = 0.9$, while Figure 9b contains the P_{fa} values versus $\rho \in [0.1, 0.9]$ for a given CNR equal to 25 dB.

The top subfigure confirms the theoretical results obtained in Section VI-B, namely that all the proposed schemes are invariant to the clutter scaling factor (at least in a clutter-dominated environment), whereas the bottom subfigure highlights the robustness of the detection thresholds with respect to variations of the covariance structure associated with the different values of ρ . Recalling that each detector is bounded from above by a statistic that is invariant to the covariance structure, these results show that the bound is tight.

C. P_d Performance and Estimation Accuracy

Now, we estimate the P_d as a function of the SINR by assuming $K_S = 24, 32$. For comparison purposes, the conventional detectors, i.e., Kelly's GLRT [35] and the

¹²It is clear that this system parameter depends on the geometry of the operating scenarios and a suitable set of guard cells can be added to account for scenario uncertainty.

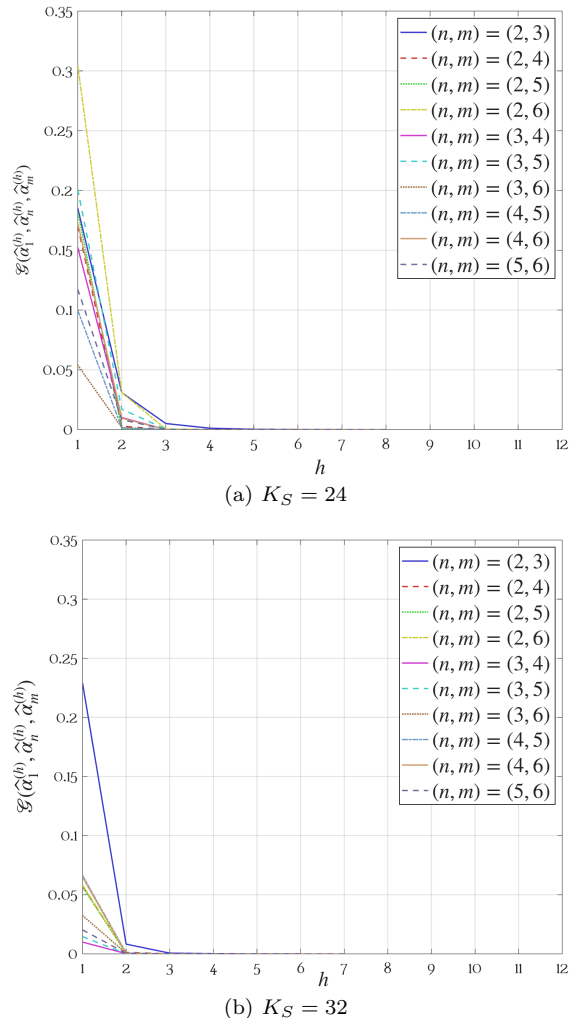


Fig. 8: Convergence analysis of the C-GLRT assuming $N = 16$ and different pairs (n, m) ; (a) $K_S = 24$, (b) $K_S = 32$.

AMF detector [29], are also included when they are fed by the range bins corresponding to either the RTR, the RTSR, or the RSTR path. Recall that these conventional detectors operate on a single range cell basis and use the nominal pointing direction of the radar (i.e., \mathbf{v}_R). Before describing the results, we recall here that the range bins 1, 3, and 6 correspond to the path RTR, RTSR (or RSTR), and RSTS, respectively.

Figure 10 shows the P_d curves for $K_S = 24$. The proposed RIS-aided schemes can significantly outperform both the conventional Kelly's GLRT and the AMF especially when they are fed by single range bins. As a matter of fact, Kelly's GLRT and the AMF fed by range cell 1 achieve $P_d > 0.9$ at around $\text{SINR} = 20$ dB, whereas the proposed schemes attain the same detection probability at $\text{SINR} = -4$ dB with a performance gain of about 24 dB. The behavior of Kelly's GLRT and AMF changes when they test cells 3 and 6. Specifically, the AMF takes advantage of both its robustness (within certain limits) to mismatched signals [38] and bistatic echo power to

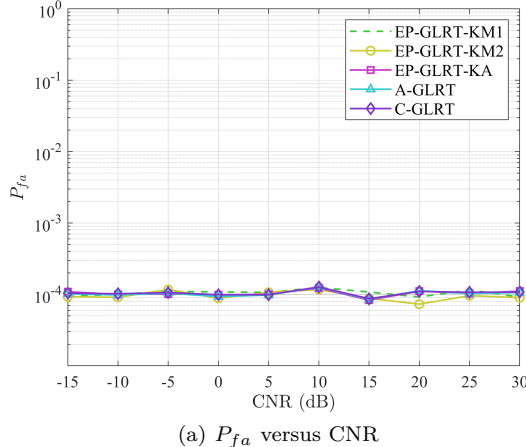
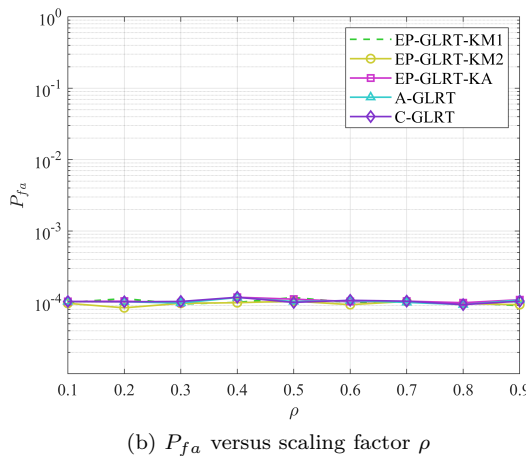
(a) P_{fa} versus CNR(b) P_{fa} versus scaling factor ρ

Fig. 9: CFAR analysis of the proposed algorithms assuming $N = 16$, $K_S = 24$, and a nominal $P_{fa} = 10^{-4}$.

improve its performance. In fact, in range cell 3, the actual target signature is \mathbf{v}_{SR} that has a lower mismatch level than \mathbf{v}_S with respect to the nominal direction \mathbf{v}_R and the target power is significantly higher than that in range cell 1. On the contrary, Kelly's GLRT is a selective decision scheme [38] and high power levels “make somehow more evident” the steering mismatch leading to poor detection performance. Indeed, when fed by range bin 3, the P_d values returned by Kelly's GLRT exhibit an upper bound around 0.6. This upper bound also depends on the estimation quality of the disturbance covariance matrix, namely on the number of training samples. As for the proposed detectors, notice that the A-GLRT, C-GLRT, and EP-GLRT-KA share almost the same performance and overcome all the other schemes with a gain of about 5 dB (at $P_d = 0.9$) over the AMF when fed by range cell 3. The performance of the EP-GLRT-KM1 and EP-GLRT-KM2 is in between that of A-GLRT and the AMF fed by range cell 3 with a gain of about 1.5 dB for the EP-GLRT-KM2 over the EP-GLRT-KM1. Two important remarks arise from these results. First, at the design stage, assuming that $\boldsymbol{\alpha}$ is known and computing the adaptive GLRT with the considered estimate of $\boldsymbol{\alpha}$ returns better

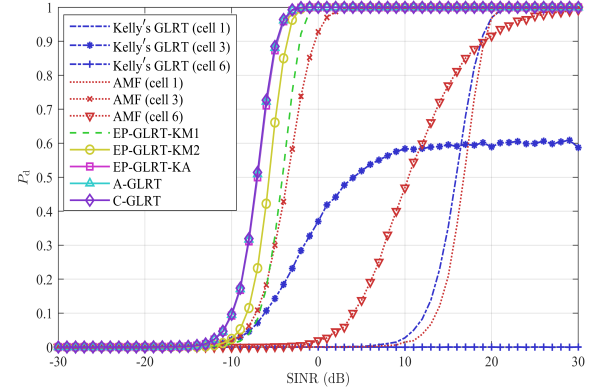


Fig. 10: P_d versus SINR assuming $N = 16$, $K_S = 24$, and $P_{fa} = 10^{-4}$.

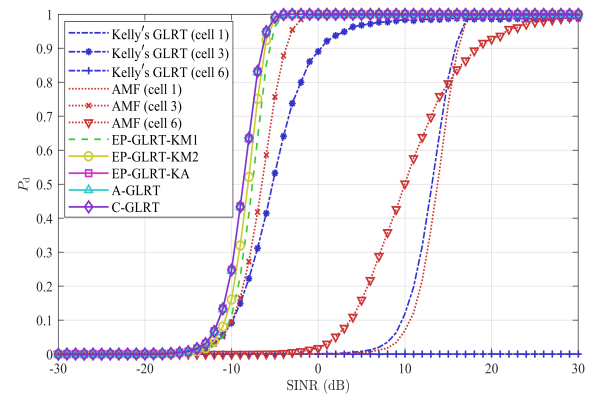


Fig. 11: P_d versus SINR assuming $N = 16$, $K_S = 32$, and $P_{fa} = 10^{-4}$.

detection performance than the adaptive GLRT obtained by assuming \boldsymbol{M} known and replacing it with the sample covariance matrix of the secondary and/or primary data. Finally, the approximation used to design the A-GLRT leads to a decision rule that is almost equivalent to the C-GLRT (for the considered simulation parameters) derived by means of an iterative procedure that converges at least to local stationary points. The impact of the amount of training data on the performance is investigated in Figure 11 where the P_d curves for all the considered architectures are estimated by assuming $K_S = 32$. As expected, a general increase of the performance occurs with the upper bound of Kelly's GLRT when fed by range cell 3 that moves from $P_d = 0.6$ to $P_d = 0.985$ (this increase is due to the large amount of secondary data). Moreover, the curves related to the proposed detectors are within an interval of about 1 dB at $P_d = 0.9$ with a gain of about 2.5 dB with respect to the AMF fed by cell 3. It is also important to point out that, if a detection is declared in cell 3 by the AMF, this would inherently correspond to a range mispositioning of the considered target. The gain with respect to the conventional schemes fed by cell 1 is still higher than 20 dB.

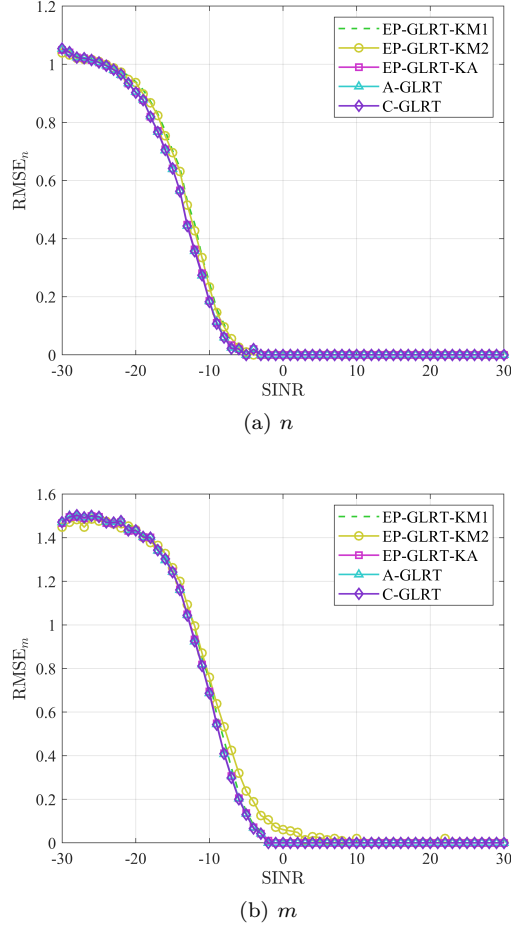


Fig. 12: RMSE versus SINR for the estimation of n and m assuming $K_S = 32$.

For the sake of completeness, we evaluate the estimation accuracy for the pairs (n, m) assuming $K_S = 32$. To this end, the performance metrics are the following estimates of the root mean square error (RMSE)

$$\begin{aligned} \text{RMSE}_n &= \sqrt{\frac{1}{N_{\text{MC}}} \sum_{k=1}^{N_{\text{MC}}} (\hat{n}_k - n)^2}, \\ \text{RMSE}_m &= \sqrt{\frac{1}{N_{\text{MC}}} \sum_{k=1}^{N_{\text{MC}}} (\hat{m}_k - m)^2}, \end{aligned} \quad (88)$$

where \hat{n}_k and \hat{m}_k denote the estimates of n and m in the k th MC trial, respectively, and $N_{\text{MC}} = 10000$ is the total number of trials. As shown in Figure 12, all the proposed detectors share almost the same estimation performance with RMSE values that decrease below 1 when $\text{SINR} > -25$ dB for n and $\text{SINR} > -15$ dB for m . Notice that the conventional detectors are not capable of estimating the positions of the echoes related to the different paths and, hence, they are not considered in this analysis.

Finally, we analyze the detection performance within a window of size $K_P = 6$ that moves over the 20 range bins of interest; we assume $K_S = 24$, and $\text{SINR} = 0$

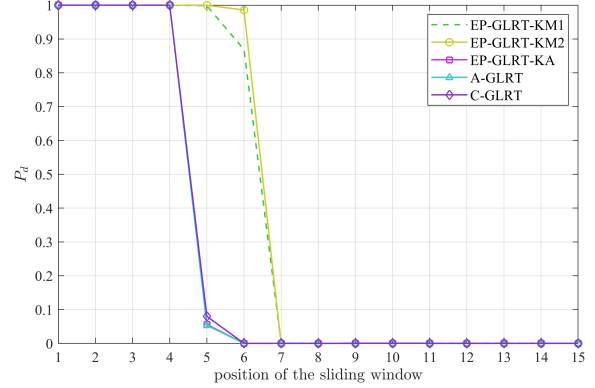


Fig. 13: P_d versus the position of the sliding window assuming $K_S = 6$ and $P_{fa} = 10^{-4}$.

dB; the last value guarantees that the proposed detectors have achieved the maximum P_d value as shown in Figure 10. This analysis has a practical value since it shows the behavior of the proposed architectures from an operating point of view. The results are reported in Figure 13 where we plot the P_d values (recall that $P_{fa} = 10^{-4}$) against the position of the first range cell belonging to the sliding window. From the inspection of the figure, it turns out that the P_d of A-GLRT, C-GLRT, and EP-GLRT-KA drops to zero when cells 1 and 3 exit from the sliding window, while for the EP-GLRT-KM1 and EP-GLRT-KM2, the P_d values quickly decrease to zero when also range bin 6 no longer belongs to the moving window. To explain this behavior, let us recall that the alternative hypothesis considers the situation where the window under test contains three range bins with target components. Thus, when the window moves, the cells contaminated by the target exit the window leading to a configuration that does not perfectly match the H_1 hypothesis. This mismatch can be the cause that induces the A-GLRT, C-GLRT, and EP-GLRT-KA to decide for H_0 when also range bin 3 exits the window, whereas EP-GLRT-KM1 and EP-GLRT-KM2 are less sensitive to this mismatch. The low sensitivity to this kind of mismatch can be a drawback because it forces the detector to declare the presence of target components in two additional cells occupied by disturbance only.

Summarizing, the above analysis has singled out the A-GLRT, C-GLRT, and EP-GLRT-KA as the most promising solutions for the detection of dim targets by exploiting the echoes reflected by a RIS that is suitably designed and deployed within the region of interest. In fact, they share almost the same performance in terms of both probability of detection and estimation accuracy overcoming the other considered decision schemes.

VII. Conclusions

The problem of detecting low-RCS targets has been addressed without resorting to neither multistatic radar

networks, with their synchronization, costs, and energy consumption issues, nor multi-frame approaches characterized by high computational costs. To this end, a search radar using a fan beam has been considered. The radar illuminates a RIS deployed in the region of interest with the aim of intercepting the energy along the irrelevant directions where the low-RCS target redirects the energy coming from the flight direction. The RIS has been designed to reflect this energy towards the radar that can capitalize most of the energy backscattered by the target. To this end, we have provided a guideline to size the RIS also suggesting possible weights for its elements. Then, we have exploited the GLRT design criterion and ad hoc modifications of it to come up with five detection architectures that can ensure the CFAR property at least with respect to the clutter power. The performance analysis has shown the effectiveness of these architectures in comparison with well-known conventional detectors. Moreover, three out of the five proposed detectors, namely the A-GLRT, C-GLRT, and EP-GLRT-KA, have arisen as the most promising solutions.

Future research tracks might encompass the use of multiple RIS deployed around the radar system to intercept more energy as well as the exploitation, at the design stage, of geometry/clutter symmetries that can reduce the number of unknown parameters to be estimated.

References

- [1] E. Björnson, O. Özdogan, and E. G. Larsson, “Reconfigurable Intelligent Surfaces: Three Myths and Two Critical Questions,” *IEEE Communications Magazine*, vol. 58, no. 12, pp. 90–96, 2020.
- [2] C. Pan, H. Ren, K. Wang, J. F. Kolb, M. Elkashlan, M. Chen, M. Di Renzo, Y. Hao, J. Wang, A. L. Swindlehurst, X. You, and L. Hanzo, “Reconfigurable Intelligent Surfaces for 6G Systems: Principles, Applications, and Research Directions,” *IEEE Communications Magazine*, vol. 59, no. 6, pp. 14–20, 2021.
- [3] Z. Fu, X. Zou, Y. Liao, G. Lai, Y. Li, and K. L. Chung, “A brief review and comparison between transmitarray antennas, reflectarray antennas and reconfigurable intelligent surfaces,” in 2022 IEEE Conference on Telecommunications, Optics and Computer Science (TOCS). IEEE, 2022, pp. 1192–1196.
- [4] F. Costa and M. Borgese, “Electromagnetic model of reflective intelligent surfaces,” *IEEE Open Journal of the Communications Society*, vol. 2, pp. 1577–1589, 2021.
- [5] D. F. Sievenpiper, J. H. Schaffner, H. J. Song, R. Y. Loo, and G. Tangonan, “Two-dimensional beam steering using an electrically tunable impedance surface,” *IEEE Transactions on antennas and propagation*, vol. 51, no. 10, pp. 2713–2722, 2003.
- [6] I. Alamzadeh, G. C. Alexandropoulos, N. Shlezinger, and M. F. Imani, “A reconfigurable intelligent surface with integrated sensing capability,” *Scientific reports*, vol. 11, no. 1, p. 20737, 2021.
- [7] L. Wu, K. Lou, J. Ke, J. Liang, Z. Luo, J. Y. Dai, Q. Cheng, and T. J. Cui, “A wideband amplifying reconfigurable intelligent surface,” *IEEE Transactions on Antennas and Propagation*, vol. 70, no. 11, pp. 10623–10631, 2022.
- [8] F. Liu, C. Masouros, A. P. Petropulu, H. Griffiths, and L. Hanzo, “Joint Radar and Communication Design: Applications, State-of-the-Art, and the Road Ahead,” *IEEE Transactions on Communications*, vol. 68, no. 6, pp. 3834–3862, 2020.
- [9] D. Li, B. Tang, X. Wang, W. Wu, and L. Xue, “Codesign for Spectral Coexistence Between RIS-Aided MIMO Radar and MIMO Communication Systems,” *IEEE Transactions on Aerospace and Electronic Systems*, vol. 60, no. 6, pp. 8166–8183, 2024.
- [10] Y. He, Y. Cai, H. Mao, and G. Yu, “RIS-Assisted Communication Radar Coexistence: Joint Beamforming Design and Analysis,” *IEEE Journal on Selected Areas in Communications*, vol. 40, no. 7, pp. 2131–2145, 2022.
- [11] X. Wang, Z. Fei, J. Guo, Z. Zheng, and B. Li, “RIS-Assisted Spectrum Sharing Between MIMO Radar and MU-MISO Communication Systems,” *IEEE Wireless Communications Letters*, vol. 10, no. 3, pp. 594–598, 2021.
- [12] Z. Liu, H. Zhang, T. Huang, F. Xu, and Y. C. Eldar, “Hybrid RIS-Assisted MIMO Dual-Function Radar-Communication System,” *IEEE Transactions on Signal Processing*, vol. 72, pp. 1650–1665, 2024.
- [13] G. Mylonopoulos, L. Venturino, E. Grossi, S. Buzzi, and C. D’Elia, “Integrated Communication and RIS-Aided Track-Before-Detect Radar Sensing,” *IEEE Open Journal of the Communications Society*, vol. 6, pp. 4519–4532, 2025.
- [14] S. Tonissen and R. Evans, “Performance of dynamic programming techniques for Track-Before-Detect,” *IEEE Transactions on Aerospace and Electronic Systems*, vol. 32, no. 4, pp. 1440–1451, 1996.
- [15] S. Tonissen and Y. Bar-Shalom, “Maximum likelihood track-before-detect with fluctuating target amplitude,” *IEEE Transactions on Aerospace and Electronic Systems*, vol. 34, no. 3, pp. 796–809, 1998.
- [16] A. Elgamal, W. Alshrafi, T. Dallmann, and P. Knott, “Enhancing polarization diversity in RIS-aided Integrated Communication and Sensing Networks,” in 2025 22nd European Radar Conference (EuRAD), 2025, pp. 307–310.
- [17] S. Buzzi, E. Grossi, M. Lops, and L. Venturino, “Radar Target Detection Aided by Reconfigurable Intelligent Surfaces,” *IEEE Signal Processing Letters*, vol. 28, pp. 1315–1319, 2021.
- [18] A. Aubry, A. De Maio, and M. Rosamilia, “Reconfigurable Intelligent Surfaces for N-LOS Radar Surveillance,” *IEEE Transactions on Vehicular Technology*, vol. 70, no. 10, pp. 10735–10749, 2021.
- [19] J. Ye, Y. Peng, P. Zhang, Q. Li, and L. Huang, “RIS-Assisted Radar NLOS Target Detection,” in 2022 5th International Conference on Information Communication and Signal Processing (ICICSP), 2022, pp. 630–635.
- [20] Z. Xie, L. Wu, J. Zhu, M. Lops, X. Huang, and M. R. B. Shankar, “RIS-Aided Radar for Target Detection: Clutter Region Analysis and Joint Active-Passive Design,” *IEEE Transactions on Signal Processing*, vol. 72, pp. 1706–1723, 2024.
- [21] S. Liaquat, I. H. Naqvi, F. A. Butt, S. Alawsh, N. M. Mahyudin, and A. H. Muqabel, “Improving SNR for NLoS Target Detection Using Multi-RIS-Assisted Monostatic Radar,” *IEEE Open Journal of Vehicular Technology*, vol. 6, pp. 774–789, 2025.
- [22] M. Rihan, E. Grossi, L. Venturino, and S. Buzzi, “Spatial Diversity in Radar Detection via Active Reconfigurable Intelligent Surfaces,” *IEEE Signal Processing Letters*, vol. 29, pp. 1242–1246, 2022.
- [23] S. Buzzi, E. Grossi, M. Lops, and L. Venturino, “Foundations of MIMO Radar Detection Aided by Reconfigurable Intelligent Surfaces,” *IEEE Transactions on Signal Processing*, vol. 70, pp. 1749–1763, 2022.
- [24] B. Wang, B. Yao, Y. Zhao, Z. Feng, and F. Hu, “Jamming Power Allocation for MIMO Radar Localization Aided by Reconfigurable Intelligent Surface,” *IEEE Transactions on Vehicular Technology*, vol. 74, no. 8, pp. 13075–13090, 2025.
- [25] E. Grossi, H. Taremizadeh, and L. Venturino, “Radar Target Detection and Localization Aided by an Active Reconfigurable Intelligent Surface,” *IEEE Signal Processing Letters*, vol. 30, pp. 903–907, 2023.
- [26] H. Zou, L. Wu, and Z. Zhang, “Target Detection for Reconfigurable Intelligent Surface Assisted MIMO Radar,” *IEEE Transactions on Vehicular Technology*, vol. 74, no. 6, pp. 9955–9960, 2025.
- [27] “Low Observable Principles, Stealth Aircraft and Anti-Stealth Technologies,” *Journal of Computations & Modelling*, vol. 4, no. 8, pp. 129–165, 2014.
- [28] S. M. Kay, *Fundamentals of Statistical Signal Processing: Detection Theory*, P. Hall, Ed., 1998, vol. 2.
- [29] F. C. Robey, D. R. Fuhrmann, E. J. Kelly, and R. Nitzberg, “A CFAR adaptive matched filter detector,” *IEEE Transactions on Aerospace and Electronic Systems*, vol. 28, no. 1, pp. 208–216, 1992.

[30] D. Orlando, G. Ricci, and L. L. Scharf, "A Unified Theory of Adaptive Subspace Detection Part I: Detector Designs," *IEEE Transactions on Signal Processing*, vol. 70, pp. 4925–4938, 2022.

[31] P. Addabbo, D. Orlando, G. Ricci, and L. L. Scharf, "A Unified Theory of Adaptive Subspace Detection Part II: Numerical Examples," *IEEE Transactions on Signal Processing*, vol. 70, pp. 4939–4950, 2022.

[32] M. A. Richards, J. A. Scheer, and W. A. Holm, *Principles of Modern Radar: Basic Principles*. Raleigh, NC: Scitech Publishing, 2010.

[33] E. Knott, J. Schaeffer, and M. Tulley, *Radar Cross Section (Second Edition)*, ser. Radar, Sonar and Navigation Series. Institution of Engineering and Technology, 2004.

[34] J. Adam, "How to design an 'invisible' aircraft," *IEEE Spectrum*, vol. 25, no. 4, pp. 26–31, 1988.

[35] E. J. Kelly, "An adaptive detection algorithm," *IEEE Transactions on Aerospace and Electronic Systems*, no. 2, pp. 115–127, 1986.

[36] E. Conte, A. De Maio, and G. Ricci, "GLRT-based adaptive detection algorithms for range-spread targets," *IEEE Transactions on Signal Processing*, vol. 49, no. 7, pp. 1336–1348, July 2001.

[37] W. Liu, J. Liu, C. Hao, Y. Gao, and Y.-L. Wang, "Multichannel adaptive signal detection: basic theory and literature review," *Science China Information Sciences*, vol. 65, no. 2, p. 121301, 2022.

[38] F. Bandiera, D. Orlando, and G. Ricci, *Advanced Radar Detection Schemes Under Mismatched Signal Models*. Switzerland AG: Springer Cham, 2009.

[39] W. Liu, W. Xie, J. Liu, and Y. Wang, "Adaptive Double Subspace Signal Detection in Gaussian Background—Part I: Homogeneous Environments," *IEEE Transactions on Signal Processing*, vol. 62, no. 9, pp. 2345–2357, 2014.

[40] O. Besson, A. Coluccia, E. Chaumette, G. Ricci, and F. Vincent, "Generalized Likelihood Ratio Test for Detection of Gaussian Rank-One Signals in Gaussian Noise With Unknown Statistics," *IEEE Transactions on Signal Processing*, vol. 65, no. 4, pp. 1082–1092, 2017.

[41] Y. Jin and B. Friedlander, "A CFAR adaptive subspace detector for second-order Gaussian signals," *IEEE Transactions on Signal Processing*, vol. 53, no. 3, pp. 871–884, 2005.

[42] P. Stoica and Y. Selen, "Cyclic minimizers, majorization techniques, and the expectation-maximization algorithm: a refresher," *IEEE Signal Processing Magazine*, vol. 21, no. 1, pp. 112–114, 2004.

[43] H. Lütkepohl, *Handbook of Matrices*. Wiley, 1997.

[44] C. Guan, S. Su, B. Wang, J. Zhong, J. Chen, F. Sun, and L. Zhan, "Electromagnetic stealth technology: A review of wave-absorbing structures," *Materials & Design*, p. 113891, 2025.

[45] D. L. Herda, J. Suryana, and A. Izzuddin, "Radar cross section of F35: Simulation and measurement," in 2020 6th International Conference on Wireless and Telematics (ICWT). IEEE, 2020, pp. 1–6.

[46] L. Gürel, H. Bağci, J.-C. Castelli, A. Cheraly, and F. Tardivel, "Validation through comparison: Measurement and calculation of the bistatic radar cross section of a stealth target," *Radio science*, vol. 38, no. 3, 2003.

[47] S. Chung, Y. Chou, and Y. Chuang, "Radar cross section analysis of stealth fighter design: Key factors and limitations of simulation," *International journal of electrical engineering*, vol. 23, no. 6, pp. 201–214, 2016.

[48] M. A. Alves, R. J. Port, and M. C. Rezende, "Simulations of the radar cross section of a stealth aircraft," in 2007 SBMO/IEEE MTT-S International Microwave and Optoelectronics Conference. IEEE, 2007, pp. 409–412.

[49] C. Kopp, "Evolving technological strategy in advanced air defense systems," *Joint Force Quarterly*, vol. 57, pp. 86–93, 2010.

[50] C. A. Balanis, *Antenna theory: analysis and design*. John wiley & sons, 2016.

[51] D. M. Pozar, S. D. Targonski, and H. Syrigos, "Design of millimeter wave microstrip reflectarrays," *IEEE transactions on antennas and propagation*, vol. 45, no. 2, pp. 287–296, 1997.

[52] M. Borgese, F. Costa, S. Genovesi, and A. Monorchio, "An iterative design procedure for multiband single-layer reflectarrays: design and experimental validation," *IEEE Transactions on Antennas and Propagation*, vol. 65, no. 9, pp. 4595–4606, 2017.

[53] F. Costa, A. Monorchio, S. Talarico, and F. M. Valeri, "An active high-impedance surface for low-profile tunable and steerable antennas," *IEEE Antennas and Wireless Propagation Letters*, vol. 7, pp. 676–680, 2008.

[54] H. Yu, P. Li, J. Su, Z. Li, S. Xu, and F. Yang, "Reconfigurable bidirectional beam-steering aperture with transmitarray, reflectarray, and transmit-reflect-array modes switching," *IEEE Transactions on Antennas and Propagation*, vol. 71, no. 1, pp. 581–595, 2022.

[55] P. Aghabeyki, Y. Cai, G. Deng, Z.-H. Tan, and S. Zhang, "A dual-polarized reconfigurable reflectarray with a thin liquid crystal layer and 2-d beam scanning," *IEEE Transactions on Antennas and Propagation*, vol. 71, no. 4, pp. 3282–3293, 2023.

[56] A. Farina and D. Orlando, "Efficient phase-only transmit beamforming: a comprehensive analysis," in 2025 IEEE 12th International Workshop on Metrology for AeroSpace (MetroAeroSpace). IEEE, 2025, pp. 122–126.